

The hidden complexity of a double-scroll attractor: Analytic proofs from a piecewise-smooth system

Cite as: Chaos 33, 043119 (2023); <https://doi.org/10.1063/5.0139064>

Submitted: 17 December 2022 • Accepted: 22 March 2023 • Published Online: 10 April 2023

 Vladimir N. Belykh,  Nikita V. Barabash and  Igor Belykh



View Online



Export Citation



CrossMark



Chaos

Special Topic: Nonlinear Model
Reduction From Equations and Data

Submit Today!

The hidden complexity of a double-scroll attractor: Analytic proofs from a piecewise-smooth system

Cite as: Chaos 33, 043119 (2023); doi: 10.1063/5.0139064

Submitted: 17 December 2022 · Accepted: 22 March 2023 ·

Published Online: 10 April 2023






View Online



Export Citation



CrossMark

Vladimir N. Belykh,^{1,2,a)}  Nikita V. Barabash,^{1,2,b)}  and Igor Belykh^{3,c)} 

AFFILIATIONS

¹Department of Mathematics, Volga State University of Water Transport, 5A, Nesterov str., Nizhny Novgorod 603950, Russia

²Department of Control Theory, Lobachevsky State University of Nizhny Novgorod, 23, Gagarin Ave., 603950 Nizhny Novgorod, Russia

³Department of Mathematics and Statistics, Georgia State University, P.O. Box 4110, Atlanta, Georgia 30302-410, USA

Note: This article is part of the Focus Issue, Non-smooth Dynamics.

^{a)}Electronic mail: belykh@unn.ru

^{b)}Electronic mail: barabash@itmm.unn.ru

^{c)}Author to whom correspondence should be addressed: ibelykh@gsu.edu

ABSTRACT

Double-scroll attractors are one of the pillars of modern chaos theory. However, rigorous computer-free analysis of their existence and global structure is often elusive. Here, we address this fundamental problem by constructing an analytically tractable piecewise-smooth system with a double-scroll attractor. We derive a Poincaré return map to prove the existence of the double-scroll attractor and explicitly characterize its global dynamical properties. In particular, we reveal a hidden set of countably many saddle orbits associated with infinite-period Smale horseshoes. These complex hyperbolic sets emerge from an ordered iterative process that yields sequential intersections between different horseshoes and their preimages. This novel distinctive feature differs from the classical Smale horseshoes, directly intersecting with their own preimages. Our global analysis suggests that the structure of the classical Chua attractor and other figure-eight attractors might be more complex than previously thought.

Published under an exclusive license by AIP Publishing. <https://doi.org/10.1063/5.0139064>

Many physical systems with symmetries exhibit spiral chaos, which is determined by a double-scroll¹ or a figure-eight attractor.² The celebrated Shilnikov spiral chaos theorem³ gives a criterion for the existence of local chaotic dynamics near a saddle-focus homoclinic orbit. However, there is a lack of computer-free analytical results related to the existence of double-scroll attractors and their global dynamical properties. Piecewise-linear and nonlinear systems of ordinary differential equations (ODEs) with double-scroll attractors are non-integrable, making such global analysis unfeasible. In this paper, we overcome this obstacle by designing a piecewise-smooth ODE system composed of three linear systems with exact solutions that generate a double-scroll attractor. We employ the system's integrability to derive a global Poincaré return map whose analysis proves the existence of the double-scroll attractor and reveals its global structure. This

complex structure contains a hidden chaotic component determined by infinite chains of horseshoes that involve interactions between all parts of the system's phase space. The similarity of geometrical properties between our system and the Chua system suggests that the classical Chua attractor and its multi-scroll analogs may have the same complex structure as their analytically tractable piecewise-smooth counterpart.

I. INTRODUCTION

Chua's circuit is a primary example of a real-world system with a double-scroll spiral attractor.¹ Chaotic dynamics and bifurcations in the piecewise-linear Chua system and its smooth analogs have been extensively studied via geometrical and computer-assisted

methods (see Refs. 4–13 as notable samples of this vast research field). Earlier rigorous results related to the chaoticity of the Chua double-scroll attractor¹ focused on proving the existence of a Shilnikov homoclinic orbit to a saddle-focus equilibrium, as this guarantees the presence of countably many saddle periodic orbits in a neighborhood of the homoclinic orbit.³ Recent work provided a computer-assisted proof of the existence of a trapping region for the double-scroll attractor in the Chua system with cubic nonlinearity.¹⁴ However, rigorous computer-free analysis of the existence and global structure of the double scroll in the Chua system remains elusive. The piecewise-linear Chua system allowed for deriving geometrical Poincaré return maps¹ associated with the attractor via compositions of eigenvectors within each linear region of its phase space;¹⁵ however, connecting the map explicitly to the system's solutions has proven to be non-feasible.

Piecewise-smooth dynamical systems with explicit solutions may offer a way to analytically prove the existence of a double-scroll attractor. However, the use of piecewise-smooth systems comes with a cost, as some fundamental theorems from the bifurcation theory of smooth ODEs may be ill-suited for non-smooth dynamics. For example, non-smooth systems can undergo local and global bifurcations that are essentially different from their smooth counterparts,^{16–20} including grazing and sliding^{21–24} (see reviews^{25,26} for more details). There also exists a body of literature on the similarity between some global bifurcations in piecewise-smooth and smooth systems,^{27,28} including a version of the Shilnikov saddle-focus theorem for Filippov systems.²⁸ Notably, several piecewise-smooth systems were constructed to prove the existence of homoclinic and heteroclinic orbits,^{27,29,30} including a Shilnikov homoclinic orbit to a saddle-focus.^{27,29} Yet, there is a lack of analytical studies of the global structure of spiral and double-scroll attractors in such systems.

In recent work,³¹ we proposed a method for designing piecewise-smooth dynamical systems with a predefined chaotic attractor and exact solutions. This method was used to construct a simple piecewise-smooth model, which switches between linear systems that yield a singular hyperbolic Lorenz-type attractor whose properties were described rigorously without any computer assistance.

In this paper, we extend this approach to the construction of an analytically tractable piecewise-smooth ODE system that switches between three linear systems with explicit solutions and generates a double-scroll attractor with geometrical properties similar to the original Chua double-scroll attractor. We derive a global Poincaré return map to prove the existence of the double-scroll attractor and explicitly characterize its global dynamical properties. In particular, we demonstrate that the double-scroll attractor corresponds to an attractor of the Poincaré map, which is confined inside four spiral strips lying on two global odd-symmetric Poincaré sections. Each Poincaré section is related to one scroll of the attractor. We first demonstrate that, at the bifurcation of a figure-eight homoclinic orbit, the four spiral strips determining the global attractor contain saddle periodic orbits associated with a countable set of classical Smale horseshoes. This result extends the Shilnikov criterion³ to the entire attractor's domain beyond the vicinity of the homoclinic orbit. We then reveal the existence of infinite-period

saddle orbits associated with a countable set of infinite chains of interacting horseshoes. In particular, these chains represent an ordered iterative process that yields sequential intersections between horseshoes related to one Poincaré section and the preimages of their counterparts from the other Poincaré section. Alternatively, these chains can generate intersections between different horseshoes and their preimages within one Poincaré section. Independent from whether one or both Poincaré sections are involved, we call such chains *multi-period* Smale horseshoes. In particular, we show that infinite-period Smale horseshoes yield a hidden set of infinite-period trajectories, including weakly stable infinite-periodic orbits that may be impossible to detect/characterize via direct numerical simulations of their Lyapunov exponents. We let the reader decide whether our definition of the hidden complexity aligns with the definition of hidden attractors³² and hidden, possibly non-smooth, dynamics.³³ Notably, the complex set of infinite-period Smale horseshoes nestled inside the double-scroll attractor partly overlaps with the classical hyperbolic of period-one Smale horseshoes. Therefore, this complex set of trajectories is well hidden; yet, it can contribute to the emergence of periodic windows of stability.

The layout of this paper is as follows. First, in Sec. II, we give the details of the model construction, discuss the phase space partition, and characterize the possible behavior of “glued” trajectories. In particular, we prove the existence of an absorbing domain that contains all of the system's attractors and derive explicit conditions on the system's parameters that guarantee that the absorbing domain does not contain sliding motions. We choose two Poincaré cross sections, each associated with one scroll of the double-scroll attractor, and prove that these cross sections are global for any attractor of the system. In Sec. III, we construct an explicit Poincaré return map. In Sec. IV, we derive the conditions under which the attractors of the map belong to four spiral strips. In Sec. V, we demonstrate that the global attractor confined inside the four spiral strips contains a chaotic component, thereby proving the existence of the double-scroll quasi-strange attractor. We introduce the concept of multi-period Smale horseshoes and use them to characterize the hidden complexity of the attractor. We also reveal the crucial role of the saddle index³⁴ in promoting the complexity of the hidden hyperbolic set of infinite-period Smale horseshoes.

II. PIECEWISE-SMOOTH SYSTEM

Inspired by the geometric construction proposed by Belykh and Chua,⁶ which yields a Poincaré map corresponding to a double-scroll attractor, we seek to construct a piecewise-smooth system amenable to an analytical treatment of its bifurcation and attractors.

A. System construction and explicit solutions

As its counterpart introduced in our previous papers^{20,31} to prove the existence of a Lorenz-type attractor and analyze its bifurcations, our piecewise-smooth system A is composed from three

linear subsystems A_0 , A_l , and A_r ,

$$\begin{aligned}
 A_0 : \quad & \dot{x} = x, \\
 & \dot{y} = -\nu y + \omega z, \\
 & \dot{z} = -\omega y - \nu z, \\
 & \text{for } (x, y, z) \in G_0, \\
 A_l : \quad & \dot{x} = -\alpha(x+h) - \Omega(z+1), \\
 & \dot{y} = -\beta y, \\
 & \dot{z} = \Omega(x+h) - \alpha(z+1), \\
 & \text{for } (x, y, z) \in G_l, \\
 A_r : \quad & \dot{x} = -\alpha(x-h) - \Omega(z-1), \\
 & \dot{y} = -\beta y, \\
 & \dot{z} = \Omega(x-h) - \alpha(z-1), \\
 & \text{for } (x, y, z) \in G_r,
 \end{aligned} \tag{1}$$

where $h, \alpha, \beta, \nu, \omega$, and Ω are positive parameters, and regions G_0 , G_l , and G_r are defined as follows:

$$\begin{aligned}
 G_0 : & |x| < h, (y^2 + z^2 \leq r^2) \cap (|z| < 1), \\
 G_l : & (z \leq -\text{sign } x, y \in \mathbb{R}^1) \setminus G_0, \\
 G_r : & (z \geq -\text{sign } x, y \in \mathbb{R}^1) \setminus G_0
 \end{aligned} \tag{2}$$

for some positive parameter $r > 1$. The partition of the phase space into three regions G_0 , G_l , and G_r with distinct dynamics determines state-dependent switching between three modes of evolution of system (1). Similar to the Chua system, the system (1) has the odd symmetry with

$$(x, y, z) \rightarrow (-x, -y, -z). \tag{3}$$

Each region G_0 , G_l , and G_r contains one fixed point, and each system A_0 , A_l , and A_r represents a normal form that describes linear dynamics around the fixed point. System A_0 has a saddle-focus fixed point $O(0, 0, 0)$ with one real ($s_1^o = 1$) and two complex eigenvalues ($s_{2,3}^o = -\nu \pm i\omega$). This fixed point has one-dimensional (1D) unstable odd-symmetric manifolds $W_{1,2}^u$ and a two-dimensional (2D) stable focus manifold W^s coinciding with the x -axis and the (y, z) -plane in region G_0 , respectively. These manifolds are further continued by trajectories of subsystem A_l (A_r) in the region G_l (G_r). In turn, subsystem A_l (A_r) has a stable focus fixed point $e_l(-h, 0, -1)$ ($e_r(h, 0, 1)$) whose trajectories are designed to return the flow of saddle-focus system A_0 back toward O (see Fig. 1). These stable foci e_l and e_r with eigenvalues $s_{1,3} = -\alpha \pm i\Omega$ and $s_2 = -\beta$ co-exist with other limit sets of system (1), including a double-scroll attractor.

The saddle-focus region G_0 is obtained from a vertical cylinder of radius r and height $2h$ by cutting its two round segments at $z = \pm 1$ (Fig. 1). Of particular importance to the argument that follows are the top and bottom faces, D_{top} ($x = h$) and D_{bot} ($x = -h$) and two vertical rectangular sides $D_r : \{|x| < h, y^2 + 1 \leq r^2, z = 1\}$ and $D_l : \{|x| < h, y^2 + 1 \leq r^2, z = -1\}$. The focus regions G_l and G_r are located outside the saddle-focus region G_0 and separated from each other by two vertical half-planes $P_l : \{x > 0, z = -1\}$ and $P_r : \{x < 0, z = 1\}$ and two parts of horizontal stripe ($x = 0, |z| \leq 1$) outside the saddle-focus part of the (y, z) -plane. All these borders of three regions G_0, G_l, G_r represent discontinuity boundaries at which system (1) switches from one mode to another. The specific choice of the discontinuity boundaries separating the modes of subsystems A_l and A_r is made to ensure that under a proper choice of parameters,

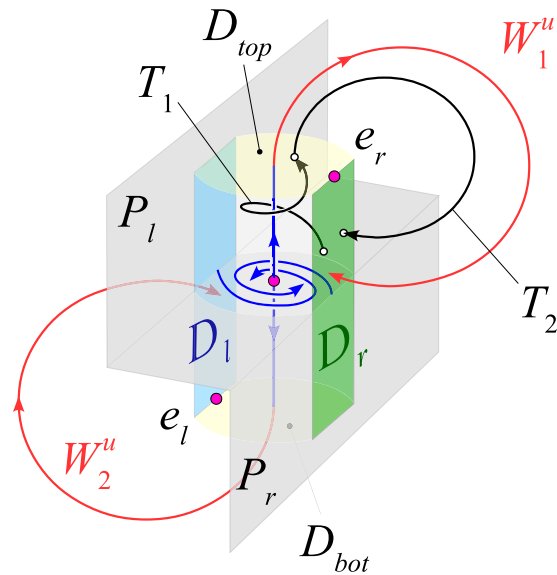


FIG. 1. Schematic diagram for the structure and dynamics of piecewise-smooth system (1). The system has a saddle-focus equilibrium at the origin and two stable foci e_r and e_l (pink circles). The phase space is partitioned into three regions with distinct linear dynamics. The wood log-shaped region with two top and bottom faces, D_{top} and D_{bot} , and vertical sides D_r (green) and D_l (blue) form the saddle-focus region. The stair-like switching manifold (gray), composed of two vertical half-planes P_l and P_r and the horizontal plane segment, separates two odd-symmetric focus regions G_l and G_r [not labeled]. The 1D unstable manifold of the saddle-focus, W_1^u [W_2^u] reaching the top [bottom] switching manifolds at D_{top} [D_{bot}] is continued by the trajectory of the focal system (red) to reach Poincaré cross section D_r (green) [D_l (light blue)]. A typical trajectory (black) starting from and returning to Poincaré cross section D_r is composed of the parts of saddle-focal and focal trajectories, corresponding to the action of the map $T = T_2 T_1$.

the top (bottom) face D_{top} (D_{bot}) is mapped by trajectories of system (1) into rectangular side D_r (D_l), making D_r and D_l global Poincaré cross sections of system (1). When designing the phase space partition (2), we were motivated to mimic the geometrical construction of a double scroll attractor from Belykh and Chua⁶ in which the top and bottom faces of a cylinder encircling the unstable 1D manifold of the saddle-focus equilibrium are mapped into the lateral surface of the cylinder. For a finite, non-infinitesimal size of the cylinder that can characterize dynamics away from a small neighborhood of the 1D unstable manifold, this would make the corresponding part of the lateral surface a round Poincaré cross section. As a result, it would not allow for the construction of an explicit global Poincaré map. For this reason, we chose to design the flat Poincaré cross sections, D_r and D_l by cutting the cylinder with two half-planes P_r and P_l . In practice, the y -size of cross sections D_r and D_l can be relatively small (Fig. 2); yet, remaining global cross sections for all trajectories of desired double-scroll attractors. This claim will be made rigorous in Subsections II B–II D.

Due to its composition from three linear systems, piecewise-smooth system (1) allows for finding all its trajectories in the form of explicit analytical solutions. That is, trajectories of system (1) are

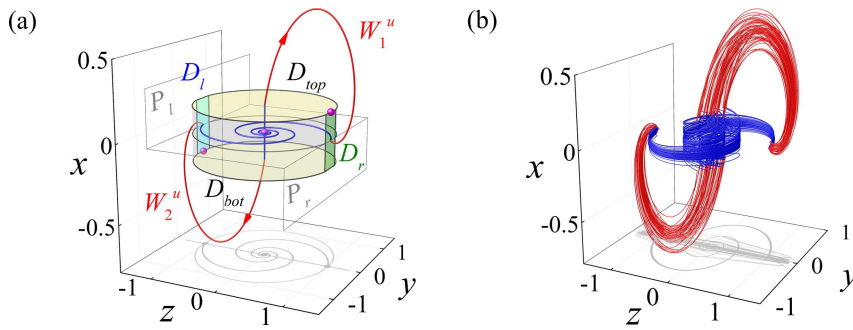


FIG. 2. Numerical illustration of the system's structure and its attractor. (a). 1D unstable manifolds of the saddle-focus equilibrium, W_1^u and W_2^u , form two odd-symmetric homoclinic orbits. (b). The corresponding double-scroll attractor. Parameters $\Omega = 1$, $\nu = 0.75$, $\omega = 3$, $h = 0.172\ 883$, $\alpha = 0.372\ 452$, $r = 1.015\ 39$, $\beta = 20$ that guarantee the existence of the homoclinic orbit are chosen from the explicit condition $\mu = 0$ (26).

“glued” from solutions of subsystems A_0 , A_l , and A_r :

$$\begin{aligned} x(t) &= x_0 e^t, \\ A_0 : y(t) &= e^{-\nu t}(y_0 \cos \omega t + z_0 \sin \omega t), \\ z(t) &= e^{-\nu t}(-y_0 \sin \omega t + z_0 \cos \omega t), \end{aligned} \tag{4}$$

$$\begin{aligned} x(t) &= -h + e^{-\alpha t}[(x_0 + h) \cos \Omega t - (z_0 + 1) \sin \Omega t], \\ A_l : y(t) &= y_0 e^{-\beta t}, \\ z(t) &= -1 + e^{-\alpha t}[(x_0 + h) \sin \Omega t + (z_0 + 1) \cos \Omega t], \end{aligned} \tag{5}$$

$$\begin{aligned} x(t) &= h + e^{-\alpha t}[(x_0 - h) \cos \Omega t - (z_0 - 1) \sin \Omega t], \\ A_r : y(t) &= y_0 e^{-\beta t}, \\ z(t) &= 1 + e^{-\alpha t}[(x_0 - h) \sin \Omega t + (z_0 - 1) \cos \Omega t], \end{aligned} \tag{6}$$

where $x_0 = x(0)$, $y_0 = y(0)$, $z_0 = z(0)$ are initial conditions.

Toward deriving an explicit Poincaré map that characterizes global dynamics of system (1), we should (i) determine the size of an absorbing domain that contains all attractors of system (1), (ii) derive the conditions under which the Poincaré cross sections D_r and D_l are global cross sections for the flow confined inside the absorbing domain, and (iii) demonstrate that the cross sections do not contain sliding motions. This analysis is detailed in Subsections II B and II C. The reader willing to accept the results of this subsection without proof can proceed to Sec. III without loss of continuity.

B. Absorbing domain

We first prove that the saddle-focus region G_0 containing cross sections D_r and D_l lies inside an absorbing domain that traps all trajectories of system (1). The existence of the absorbing domain and its dependence on the system's parameters are specified in the following statement.

Theorem 1 (Existence of an absorbing domain): A. For $\alpha \leq \alpha_h$, where

$$\alpha_h = -\frac{2\Omega}{3\pi} \ln h, \tag{7}$$

the system (1) has an absorbing domain bounded by a stable limit cycle C_1 which crosses the point $(x = x_c, y = 0, z = -1)$, where

$x_c \geq h$ is a unique root of the equation

$$x + h - \sqrt{(x - h)^2 + 4} \exp\left(-\frac{\alpha}{\Omega} \left(\pi + \arctan \frac{2}{x - h}\right)\right) = 0. \tag{8}$$

The limit cycle C_1 with its 2D cylindrical submanifold encircles the saddle-focus region G_0 and attracts all trajectories from the cycle's outer side [Figs. 3(a) and 3(b)].

B. For $\alpha > \alpha_h$, the absorbing domain is bounded by the union of the trajectories, starting from points $(x = \pm h, |y| < r, z = \mp 1)$ and the rectangles $(-h < x < -\eta(h), |y| < r, z = 1)$, $(\eta(h) < x < h, |y| < r, z = -1)$ [see Fig. 3(c)].

Proof. The dynamics outside of the saddle-focus region G_0 are described by the focal systems A_l and A_r whose uncoupled y equation, $\dot{y} = -\beta y$, guarantees the existence of the stable invariant manifold $y = 0$. Therefore, any limit cycle or a trajectory lying outside of G_0 must (i) belong to this invariant manifold and (ii) have a stable 2D cylindrical manifold. Therefore to prove Part A, it is sufficient to show that trajectories in the (x, z) plane form a stable limit cycle which determines the size of the absorbing domain. Toward this goal, we first construct the map $x \rightarrow -\eta(x) : (x \geq h, y = 0, z = -1) \rightarrow (x < 0, y = 0, z = +1)$ which determines how a point from the half-plane P_l , corresponding to positive $x \geq 0$ is mapped into P_r corresponding to negative x via a trajectory of the focal system A_r . In turn, a trajectory of the focal system A_l subsequently maps the point $x < 0$ from the half-plane P_r back to P_l via the map $x \rightarrow -\eta(x) : (x < 0, y = 0, z = -1) \rightarrow (-\eta(x) > 0, y = 0, z = -1)$. Due to the odd-symmetry of system (1), the resultant second-iterate map $x \rightarrow x : -\eta(-\eta(x)) = \eta(\eta(x))$. Hence, a stable fixed point of the first-iterate map $\eta(x)$ is also a stable fixed point of the second-iterate map $\eta(\eta(x))$, which corresponds to a stable limit cycle in the system (1). Note that the first-iterate map $\eta(x)$ always yields positive values of x and therefore is more convenient to analyze than the original first-iterate map $-\eta(x)$.

To derive the explicit form of the map $\eta(x)$, we use the explicit solutions (6) of system A_r with initial conditions $(x(0) \geq h, y(0) = 0, z(0) = -1)$:

$$\begin{aligned} x(t) &= h + e^{-\alpha t}[(x(0) - h) \cos \Omega t + 2 \sin \Omega t], \\ z(t) &= 1 + e^{-\alpha t}[(x(0) - h) \sin \Omega t - 2 \cos \Omega t], \end{aligned} \tag{9}$$

and boundary conditions $x(\tau) = \eta(x) \equiv -\bar{x}, y = 0, z(\tau) = 1$, where τ is the transition time from P_l to P_r . Hereafter, the bar denotes the subsequent iterate of x . Substituting the boundary conditions

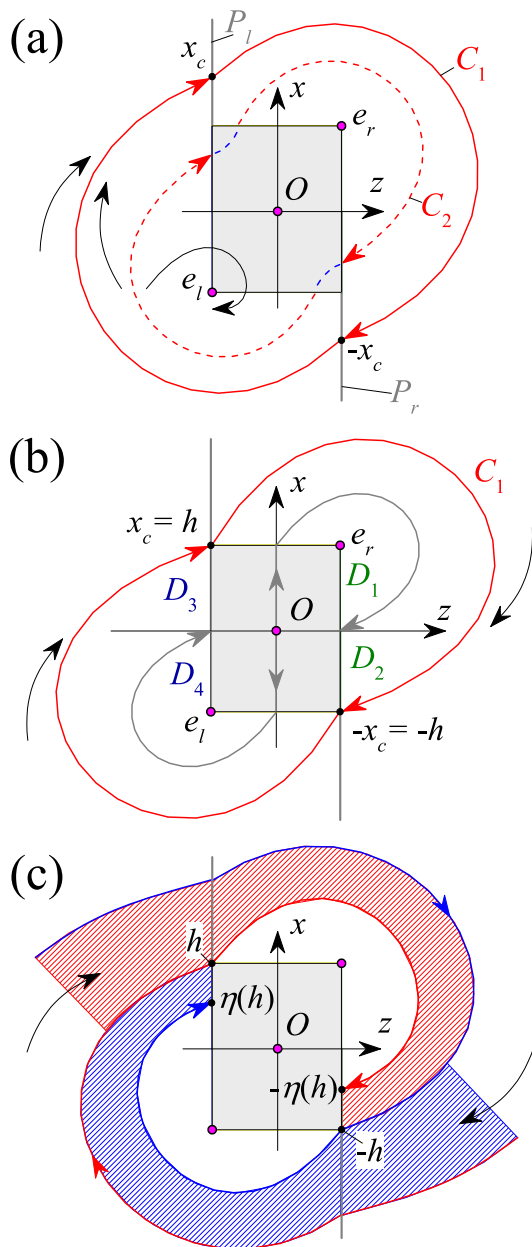


FIG. 3. Absorbing domain (illustration of Theorem 1). The xz projection of the phase space of (1) at $y = 0$. The shaded square is the projection of the saddle-focus region G_0 . (a). $\alpha > \alpha_h$. Stable limit cycle C_1 (red solid line) attracts all outer trajectories of the system and determines the absorbing domain. The saddle limit cycle C_2 separates the basins of attraction of C_1 and the double-scroll attractor. (b). $\alpha = \alpha_h$. Stable cycle C_1 borders the saddle-focus region G_0 . Saddle limit cycle C_2 not shown. The stable manifolds of saddle O form a figure-eight homoclinic orbit, encircling stable foci e_l and e_r . (c). $\alpha < \alpha_h$. The absorbing domain is formed by the saddle-focus region (shaded square) and two adjacent white regions bounded by trajectories R and L [not labeled]. The red and blue shaded “rivers” form the channels for outer trajectories to enter the absorbing domain. Limit cycles C_1 and C_2 lie inside the absorbing domain and are not shown.

into (9), we turn the z -equation into $(x(0) - h) \sin \Omega \tau - 2 \cos \Omega \tau = 0$. Therefore, the transition time $\tau = (\pi + \arctan \frac{2}{x(0)-h}) / \Omega$. Similarly, the x -equation in (9) becomes $\bar{x} = -x(\tau) = -h - e^{-\gamma(\pi + \arctan \frac{2}{x(0)-h})} [(x(0) - h) \cos \Omega \tau + 2 \sin \Omega \tau]$, where $\gamma = \frac{\alpha}{\Omega}$ and $(x(0) - h) \cos \Omega \tau + 2 \sin \Omega \tau = \frac{1}{2}((x(0) - h)^2 + 4) \sin \Omega \tau$. In turn, by a simple trigonometric identity, the factor $\sin \Omega \tau = \sin(\pi + \arctan \frac{2}{x(0)-h}) = -\frac{2}{\sqrt{(x(0)-h)^2 + 4}}$. Collecting the terms and replacing the initial condition $x(0)$ with x , we obtain the map $\eta(x)$:

$$\bar{x} = \eta(x) = -h + E(x)\sqrt{(x - h)^2 + 4},$$

$$E(x) = \exp(-\gamma(\pi + \arctan(\frac{2}{x - h}))),$$
(10)

where $\gamma = \frac{\alpha}{\Omega}$.

To prove that the map (10) has a stable fixed point, we calculate the first and second derivatives of $\eta(x)$ which are

$$\eta' = \frac{E(x)}{\sqrt{(x - h)^2 + 4}}((x - h) + 2\gamma) > 0,$$

$$\eta'' = \frac{4E(x)}{((x - h)^2 + 4)^{\frac{3}{2}}}(1 + \gamma^2) > 0$$
(11)

in the considered range of $x \geq h$. From (11) we conclude that the first derivative $\eta'(x)$ monotonically increases and is less than 1 for any $x \in [h, \infty)$ since

$$\eta'(h) = \gamma e^{-\frac{3\pi\gamma}{2}} < \eta'(x) < e^{-\gamma\pi} = \eta'(\infty) < 1, x \in [h, \infty). \quad (12)$$

Therefore, if $\eta(x = h) = -h + 2e^{-\frac{3\pi\gamma}{2}} \geq h$ which is true if $\alpha \leq \alpha_h = -\frac{2\Omega}{3\pi} \ln h$, yielding the condition (7), then the graph of $\eta(x)$ starting from $x = h$ intersects the diagonal line $\bar{x} = x$ at a point x_c with $\eta'(x_c) < 1$. Hence, x_c is a unique stable fixed point of the map (10), corresponding to a stable limit cycle C_1 of the original model (1) which crosses the point $(x = x_c, y = 0, z = -1)$. The actual value of the fixed point x_c can be formally found from solving the Eq. (10) with \bar{x} replaced with x , yielding the transcendental Eq. (8). The limit cycle C_1 with its 2D cylindrical manifold is a global attractor for all trajectories from its outer side, and therefore defines an absorbing domain of system (1). This completes the proof of Part A.

For $\alpha > \alpha_h$, the limit cycle C_1 enters into the saddle-focus region G_0 and its existence cannot be accessed via the map (10). Instead, we pay particular attention to two families of trajectories which start from the points $(x(0) = h, |y(0)| < r, z(0) = -1)$ in the half-plane P_l and from the points $(x(0) = -h, |y(0)| < r, z(0) = +1)$ in the half-plane P_r . For definiteness, we consider trajectory R starting from point $p_R : (x(0) = h, y(0) = 0, z(0) = -1)$ and trajectory L starting from point $p_L : (x(0) = -h, y(0) = 0, z(0) = +1)$ as representatives of the two families. Due to the contracting properties of the map (10), the point p_R is mapped by trajectory R of the focal system A_r , into the point $\bar{p}_R : (x = -\eta(h), y(0) = 0, z(0) = +1)$ with $\eta(h) < x(0) = h$. Similarly, the point p_L is mapped by trajectory L of the focal system A_l , into the point $\bar{p}_L : (x = \eta(h), y(0) = 0, z(0) = -1)$. At these instants, trajectories R and L enter the saddle-focus region G_0 and are continued via

the saddle-focus system A_0 to eventually leave G_0 and reach the half-planes P_l and P_r , respectively. Note that the point \bar{p}_R in the half-plane P_r is mapped into the point $\bar{p}_R : (x < \eta(h), y(0) = 0, z(0) = -1)$ which must be located below the point \bar{p}_L with $x = \eta(h)$ since the continuation of trajectory R in G_0 and G_l is encircled by the trajectory L . Similarly, the point \bar{p}_L in the half-plane P_l is mapped into the point $\bar{p}_L : (-x < -\eta(h), y(0) = 0, z(0) = +1)$. Hence, the trajectories R, L and two segments $(\eta(h) < x < h, y = 0, z = -1)$ and $(-h < x < -\eta(h), y = 0, z = 1)$ form a trapping region for all trajectories with $y = 0$ located inside of it. This trapping region is also an absorbing domain for all outer trajectories with $y = 0$ that must be confined inside the “rivers” formed by the trajectories starting from points $(x(0) = -h, y(0) = 0, z(0) = +1)$ and $(x(0) = h, y(0) = 0, z(0) = -1)$ in reverse time. The flow inside the rivers, defined by the stable focal systems A_l and A_r , guides the trajectories to eventually enter the absorbing domain via the two segments $(\eta(h) < x < h, y = 0, z = -1)$ and $(-h < x < -\eta(h), y = 0, z = 1)$. Extending this argument to all trajectories from the two families with $|y| < r$, we arrive at the statement of Part B. \square

Remark 1: Note that the limit cycle C_1 , determining the size of the absorbing domain for $\alpha \geq \alpha_h$ lies only in the region $G_l \cup G_r$ and attracts all outer and inner trajectories from $G_l \cup G_r$. However, the inner trajectories from $G_l \cup G_0 \cup G_r$, composed of focal and saddle pieces are not determined by the map (10) and do not necessarily approach the limit cycle C_1 . There must exist a saddle limit cycle $C_2 \in G_l \cup G_0 \cup G_r$ which separates the limit cycle C_1 and stable foci e_1 and e_2 [Fig. 3(a)].

C. Sliding motions

The piecewise-smooth system (1) has sliding motions. Our goal is to single out the system’s parameters for which (i) the system does not have stable sliding motions and (ii) unstable sliding motions lie outside the absorbing domain and do not play any role in the formation of the double-scroll attractor.

The borders of three regions G_0, G_l, G_r partitioning the phase space and representing the discontinuity boundaries of system (1) are natural suspects for containing sliding motions. We start by examining them one by one. Denote the discontinuity boundary of the saddle-focus region G_0 by ∂G_0 and its inner and outer sides by G_0^- and G_0^+ , respectively. Recall that the boundary $\partial G_0 = D_{top} \cup S \cup D_{bot}$ is composed from the top D_{top} and bottom D_{bot} disks and the lateral surface $S = D_l \cup S_0 \cup D_r$, where $S_0 = (y^2 + z^2 = r^2, |x| < h, |z| < 1)$ is the cylindrical part of S .

Statement 1 (Sufficient conditions for the absence of sliding motions in the attractor): *The discontinuity boundary ∂G_0 of the saddle-focus region G_0 does not contain sliding motions if the parameters satisfy the conditions*

$$\begin{aligned} \sqrt{r^2 - 1} &< \frac{\nu}{\omega}, \\ \beta &> \frac{\Omega h + \alpha}{r^2 - 1}, \end{aligned} \tag{13}$$

such that the trajectories of system (1) reaching the region G_0 enter it through the surface S and leave the region G_0 through the disks D_{top} and D_{bot} .

Proof. To prove the claim of Statement 1, it is sufficient to find the conditions under which the vector fields $(\dot{x}, \dot{y}, \dot{z})$ of systems A_0, A_l and A_r are pointing in the same direction at the inner and outer sides G_0^-, G_0^+ of ∂G_0 . Indeed, the vector field at the inner and outer sides D_{top}^- and D_{top}^+ of D_{top} is oriented outside G_0 since $\dot{x}|_{D_{top}^-} = h > 0$ and $\dot{x}|_{D_{top}^+} = \Omega(1 - z) > 0$. Due to the symmetry, the same claim applies to the bottom disk D_{bot} with $\dot{x}|_{D_{bot}^-} < 0$ and $\dot{x}|_{D_{bot}^+} < 0$. The vector field at the outer side of rectangles D_l and D_r is defined by the focal systems A_l and A_r , respectively, and is always oriented inside G_0 as $\dot{z}|_{z=-1} = \Omega(h + x) > 0$ and $\dot{z}|_{z=1} = -\Omega(h - x) < 0$ for $|x| < h$. At the same time, the vector field at the inner side of D_l and D_r is governed by system A_0 and also oriented inside G_0 if

$$\dot{z}|_{z=-1} = -\omega y + \nu > 0, \quad \dot{z}|_{z=1} = -\omega y - \nu < 0. \tag{14}$$

$|y| \leq \sqrt{r^2 - 1}$ on both D_l and D_r and hence, the inequality (14) is fulfilled under the first condition in (13). Finally, we need to prove that the vector fields at the inner and outer sides of cylindrical lateral surface S_0 are oriented inside S_0 . This can be done by considering S_0 as a level surface of a directing Lyapunov function $V = \frac{y^2}{2} + \frac{z^2}{2}$ and demonstrating that $\dot{V}|_{S_0^\mp} < 0$ along the trajectories of system A_0 and A_r (or A_l), respectively. Taking into account that $y^2 = r^2 - z^2$ at S_0 , we obtain the inequalities to satisfy

$$\dot{V}|_{S_0^-} = y\dot{y} + z\dot{z}|_{S_0^-} = -\nu r^2 < 0, \tag{15}$$

for A_0 , and

$$\dot{V}|_{S_0^+} = -(r^2 - z^2)\beta - \alpha z^2 + [\alpha - \Omega(h - x)]z < 0, \tag{16}$$

for A_r . The condition (15) holds true for any r and positive ν . The condition (16) is fulfilled if

$$\frac{[\alpha - \Omega(h - x)]z - \alpha z^2}{r^2 - z^2} < \beta$$

which can be estimated as

$$\frac{[\alpha - \Omega(h - x)]z - \alpha z^2}{r^2 - z^2} < \frac{\alpha + h\Omega}{r^2 - 1} < \beta,$$

where the right-hand side inequality is the second condition in (13). \square

To complete the description of possible sliding motions on the other discontinuity boundaries beyond the saddle-focus region G_0 , we note that (i) the strip $(x = 0, |z| < 1, y^2 > r^2 - z^2)$ contains unstable sliding motions and (ii) the parts of the half-planes $P_l \setminus D_l$ and $P_r \setminus D_r$ are passable for the trajectories of system (1). The statement directly follows from the orientation of the vector fields of systems A_l and A_r at these discontinuity boundaries.

D. Global Poincaré cross section

It follows from Theorem 1 that for $\alpha > \alpha_h$ all trajectories of system (1) reach the lateral surface S of the saddle-focus region G_0 . Moreover, Statement 1 guarantees that under conditions (13), these trajectories (with the exception of stable foci $e_l, e_r \in G_0$) transversely cross the lateral surface S since its boundary has no sliding motions. The vertical x -flow inside G_0 is governed by the first equation of

saddle-focus system A_0 . As a result, the trajectories leave the saddle-focus region via the top and bottom sections D_{top} and D_{bot} to be returned by the focal systems A_r and A_l back to S , making it a global Poincaré cross section.

Toward our goal of deriving an explicit global Poincaré return map, we need to impose additional constraints on the parameters that guarantee that the vertical sides D_l and D_r , of the lateral surface S are global Poincaré cross sections for all non-trivial attractors of system (1). This amounts to requiring a sufficiently strong contraction in the y direction so that any trajectory starting from D_{top} (D_{bot}) and returning to the lateral surface S does not miss its flat side D_r (D_l).

Theorem 2 (Global cross section): *The union of rectangles $D = D_l \cup D_r$ is a global cross section for any attractor of system (1) if the parameters satisfy the conditions*

$$\alpha \geq \alpha_h = -\frac{2\Omega}{3\pi} \ln h, \tag{17a}$$

$$\beta > \frac{\Omega h + \alpha}{r^2 - 1}, \tag{17b}$$

$$r \exp\left(\frac{-3\pi\beta}{2\Omega}\right) < \sqrt{r^2 - 1} < \frac{\nu}{\omega}. \tag{17c}$$

Proof. By the system's construction, its trivial attractors, stable foci e_l and e_r , lie in the planes D_l and D_r , respectively. The inequality (17a) comes from Part B of Theorem 1 which guarantees that the entire saddle-focus region G_0 , including D_l and D_r , belongs to the absorbing domain. The inequality (17b) and the right-hand side of (17c) are the conditions of Statement 1 which, in particular, provide sufficient conditions for the sections D_l and D_r to contain no sliding motions. As a result, all trajectories starting from the lateral surface S of G_0 , including D_l and D_r will enter G_0 and reach D_{top} and D_{bot} due to $\dot{x} = x$ in the saddle-focus system A_0 . Therefore, $D = D_l \cup D_r \rightarrow D_{top} \cup D_{bot}$. To complete the loop, we need to prove that $D_{top} \cup D_{bot} \rightarrow D = D_l \cup D_r$. Hence, we consider the mapping of D_{top} into half-plane $P = (x < h, y \in \mathbb{R}^1, z = 1)$ (the mapping D_{bot} to $(x > -h, y \in \mathbb{R}^1, z = -1)$ has the same properties due to system's symmetry). Note that D_{top} is mapped into P_r by the trajectories of focal system A_r whose y -coordinates are governed by $y(t) = y(0)e^{-\beta t}$, where $y(0) \in [-r, r]$ is the y initial condition in D_{top} . These trajectories reach P_r in time $\tau = \frac{3\pi}{2\Omega}$ and have the coordinates $y(\tau) = y(0)e^{-\frac{3\pi\beta}{2\Omega}}$. The details of the explicit calculation of τ will be given in Sec. III [see Eq. (24)]. We require $y(\tau)$ to fall within the y dimension of D_r such that $|y(\tau)| < \sqrt{r^2 - 1}$, yielding the left-hand side inequality in (17c). Similarly, we require $x(\tau)$ to fall within the x dimension of D_r . Given the fact that the (xz) -equations of system A_r do not depend on y , this requirement yields $|x(\tau)| = |h - 2e^{-\frac{3\pi\alpha}{2\Omega}}| < h$ which leads to the inequality (17a), coinciding with the condition of Part B in Theorem 1. \square

III. POINCARÉ RETURN MAP: THE CONSTRUCTION

We follow the steps of our recent study³¹ and derive a flow-defined explicit Poincaré return map which allows for proving the

existence of a double-scroll attractor and characterizing its structure. To construct the Poincaré map, we choose the global two-part cross section D , composed of D_l and D_r , and analyze how this cross section is mapped into itself by trajectories of $A_0, A_{l,r}$. This amounts to defining a mapping $T : D \rightarrow D$ as a composition $T = T_2 T_1$ with

$$T_1 : \begin{cases} D_{1,3} \rightarrow D_{top}, \\ D_{2,4} \rightarrow D_{bot}, \end{cases} \tag{18}$$

$$T_2 : \begin{cases} D_{top} \rightarrow D_r, \\ D_{bot} \rightarrow D_l, \end{cases} \tag{19}$$

where the cross section D_r (D_l) is divided into two symmetrical parts $D_1 = D_r|_{x \geq 0}$, $D_2 = D_r|_{x < 0}$ ($D_3 = D_l|_{x \geq 0}$, $D_4 = D_l|_{x < 0}$) by the saddle-focus O and its stable 2D manifold [see Fig. 3(b)].

We first derive the map T_2 which is generated by the trajectories of the saddle-focus system A_0 that transfer points from D_r and D_l to the top and bottom sections, D_{top} and D_{bot} . Using solutions (4) of system A_0 with the initial conditions $(x(0), y(0), z(0)) \in D_{l,r}$ and final boundary conditions $(x(\tau_1), y(\tau_1), z(\tau_1)) \in D_{top}$ for $x(0) > 0$ and $(x(\tau_1), y(\tau_1), z(\tau_1)) \in D_{bot}$ for $x(0) < 0$, we obtain

$$x(\tau_1) = x(0)e^{\tau_1},$$

$$y(\tau_1) = e^{-\nu\tau_1} (y(0) \cos \omega\tau_1 + z(0) \sin \omega\tau_1), \tag{20}$$

$$z(\tau_1) = e^{-\nu\tau_1} (-y(0) \sin \omega\tau_1 + z(0) \cos \omega\tau_1),$$

where τ_1 is the travel time from $D_{l,r}$ to D_{top} or D_{bot} . From the first equation of (20) and the boundary condition $|x(\tau_1)| = h$, we calculate the travel time

$$\tau_1 = -\ln \frac{|x(0)|}{h}. \tag{21}$$

Substituting τ_1 into the y and z equations of (20), we derive the map T_1 :

$$\begin{aligned} y(\tau_1) &= \frac{|x(0)|^\nu}{h^\nu} \left(y(0) \cos \left(\omega \ln \frac{|x|}{h} \right) - z(0) \sin \left(\omega \ln \frac{|x|}{h} \right) \right), \\ z(\tau_1) &= \frac{|x(0)|^\nu}{h^\nu} \left(y(0) \sin \left(\omega \ln \frac{|x|}{h} \right) + z(0) \cos \left(\omega \ln \frac{|x|}{h} \right) \right). \end{aligned} \tag{22}$$

We then construct the map T_1 which maps the disk D_{top} into D_r by the trajectories of the focal system A_r (the mapping of D_{bot} into D_l by the trajectories of the focal A_l is odd symmetric). Analyzing the solutions (6) with initial conditions $(x(\tau_1) = h, y(\tau_1), z(\tau_1))$ in D_{top} and boundary conditions $(x(\tau_2), y(\tau_2), z(\tau_2))$ in D_r , we obtain the explicit form of map T_2 :

$$x(\tau_2) = h - e^{-\alpha\tau_2} (z(\tau_1) - 1) \sin \Omega\tau_2,$$

$$y(\tau_2) = y(\tau_1)e^{-\beta\tau_2}, \tag{23}$$

$$z(\tau_2) = 1 + e^{-\alpha\tau_2} (z(\tau_1) - 1) \cos \Omega\tau_2,$$

where τ_2 is the travel time from D_{top} to D_r . Solving the third equation of (23) with the boundary condition $z(\tau_2) = 1$ yields $\cos \Omega\tau_2 = 0$ with $\tau_2 = \frac{(2k-1)\pi}{2\Omega}$, where $k = 1, 2, \dots$ corresponds to the instances at which the focal trajectory intersects the plane $z = 1$. The first instance with $k = 1$ yields the first equation of (23) with $\sin \Omega\tau_2 = 1$.

Therefore, at this instance $x > h$ and the trajectory first crosses the plane $z = 1$ at a point located above the cross section D_r which is irrelevant to the desired travel time τ_2 to D_r . In fact, the trajectory reaches D_r at $k = 2$ which corresponds to $\sin \Omega\tau_2 = -1$ and $x(\tau_2) < h$. Thus, the travel time is

$$\tau_2 = \frac{3\pi}{2\Omega}. \tag{24}$$

Completing the loop, from (20), (21), (23), and (24), we obtain the Poincaré return map $D_{1,3} \rightarrow D_r$:

$$\begin{aligned} \bar{x} = & h - e^{-\frac{3\pi\alpha}{2\Omega}} + e^{-\frac{3\pi\alpha}{2\Omega}} \left(\frac{|x|}{h}\right)^v \left(y \sin\left(\omega \ln \frac{|x|}{h}\right) \right. \\ & \left. + z \cos\left(\omega \ln \frac{|x|}{h}\right)\right), \end{aligned} \tag{25}$$

$$\bar{y} = e^{-\frac{3\pi\beta}{2\Omega}} \left(\frac{|x|}{h}\right)^v \left(y \cos\left(\omega \ln \frac{|x|}{h}\right) - z \sin\left(\omega \ln \frac{|x|}{h}\right)\right),$$

where once again the bar denotes the subsequent iterate of the map. The mapping $D_{2,4} \rightarrow D_l$ is obtained from (25) by the odd-symmetric involution of the variables.

Finally, after the following re-scaling of x and introduction of new parameters

$$\frac{x}{h} \rightarrow x, \quad \mu = 1 - \frac{1}{h} \exp\left(-\frac{3\pi\alpha}{2\Omega}\right), \quad q = \exp\left(-\frac{3\pi\beta}{2\Omega}\right), \tag{26}$$

and taking into account the odd symmetry of system (1), we derive the explicit Poincaré return map $T = T_2 T_1$ of the global cross section into itself $D \rightarrow D$:

$$\begin{aligned} \bar{x} = & \mu \text{sign}(x) + (1 - \mu)|x|^v \left(y \sin(\omega \ln |x|) + z \cos(\omega \ln |x|)\right), \\ \bar{y} = & q|x|^v \left(y \cos(\omega \ln |x|) - z \sin(\omega \ln |x|)\right), \\ \bar{z} = & \text{sign}(x). \end{aligned} \tag{27}$$

Note that despite the presence of the z variable, system (27) is effectively a 2D mapping, since the z equation only controls the switch between two cross sections D_l ($z = -1$) and D_r ($z = 1$). As a result, the variable z in the first two equations of (27) only takes the values ± 1 .

The map (27) is discontinuous at $x = 0$ as the segments

$$\begin{aligned} l'_0 = & \left(x = 0, |y| < \sqrt{r^2 - 1}, z = -1\right) \in D_l \\ l''_0 = & \left(x = 0, |y| < \sqrt{r^2 - 1}, z = 1\right) \in D_r \end{aligned} \tag{28}$$

are mapped into the saddle-focus O and therefore points from l'_0 and l''_0 do not return back to the cross section $D = D_l \cup D_r$ (Fig. 4). However, points from a vicinity of segments l'_0 and l''_0 return to D , closely passing by the saddle-focus O . Therefore, by continuity, we can define the map (27) at the discontinuity lines l'_0 and l''_0 as

$$\bar{l}'_0, \bar{l}''_0 : \begin{cases} (\bar{x}, \bar{y}, \bar{z}) = M_l(-\mu, 0, -1) & \text{for } x \rightarrow -0, \\ (\bar{x}, \bar{y}, \bar{z}) = M_r(\mu, 0, 1) & \text{for } x \rightarrow +0. \end{cases} \tag{29}$$

Here, the point M_l (M_r) is the intersection of the cross section D_l (D_r) with the one-dimensional unstable manifold W^u_2 (W^u_1) of O .

Notice that parameter $\mu = 0$ corresponds to the formation of a figure-eight homoclinic orbit to the saddle-focus O which is represented by the singularity point ($x = 0, y = 0$). Hence, it follows from (26), that $\alpha_h = -\frac{2\Omega}{3\pi} \ln h$ is the explicit condition for the existence of the figure-eight homoclinic orbit. Deriving such an explicit condition is out of reach for the Chua system or its smooth analogs with double-scroll attractors. The homoclinic orbit formed by the saddle-focus and focal parts of the piecewise-smooth trajectory and existing at $\mu = 0$ is depicted in Figs. 1, 2(a), and 3(b).

Remarkably, for $\mu = 0$ and $x > 0$, the one-side map (27) with $z = 1$ becomes the classical Shilnikov map³⁵ which characterizes the complex local dynamics in a small neighborhood of a saddle-focus homoclinic orbit in a system with a one-scroll spiral attractor.³⁴ The full map (27), derived from the analytically tractable system (1), possesses an unusual power for describing the global dynamics inside the entire absorbing domain with large x and y , far from the homoclinic orbit, and proving the existence of the system's attractors.

The map (27) is a flow-defined analog of the one suggested in Belykh and Chua⁶ which maps the entire cylindrical surface S into itself in a geometrical model of a double-scroll attractor. The map⁶ used the combination of the x coordinate and the phase coordinate $\phi \in [0, 2\pi]$ around the cylinder to characterize the mapping $S \rightarrow S$. However, in contrast to (27), the map⁶ could not be explicitly related to the global dynamics of a concrete flow-defined ODE system with a double-scroll attractor. The curvature of the cylindrical surface S represented the major obstacle to deriving such an explicit global map. This is due to the fact that the corresponding boundary for calculating the travel time τ_2 from D_{top} to S would be curved, making such explicit calculations non-feasible. A way out of this dilemma could be in considering a small fragment of the lateral surface S around the homoclinic orbit as a flat Poincaré section with infinitesimal x and y . However, such a map is limited to the local behavior of trajectories in a small neighborhood of the homoclinic orbit and cannot be used to describe the structure of the double-scroll attractor in the entire phase space.

The conditions of Theorem 2 for the existence of the global cross section D can be formulated in terms of the parameters of map (27) via (17a) and (17c):

$$0 \leq \mu < 1, \quad 0 < q < \sqrt{1 - \frac{1}{r^2}}, \tag{30}$$

where $\sqrt{1 - \frac{1}{r^2}}$ must satisfy the condition (17b).

The Jacobian determinant of map (27) is given by

$$J = (1 - \mu)q|x|^{2v-1}(v + \omega y)z. \tag{31}$$

As the global cross section $D = D_l \cup D_r$ is defined in the region $|y| < \sqrt{r^2 - 1}$, then due to (17c) the cofactor $(v + \omega y) > 0$. Thus, the Jacobian determinant is positive for $z = 1$ and negative for $z = -1$. The latter property is dictated by our choice of the same (global) coordinate of systems A_l and A_r so that both cross sections D_l and D_r have the same normal vector $(0, 0, 1)$. This choice allows for writing the map (27) in its compact form, without the need for introducing additional signum terms or breaking the equations into two maps for systems for D_l and D_r , corresponding to the normal

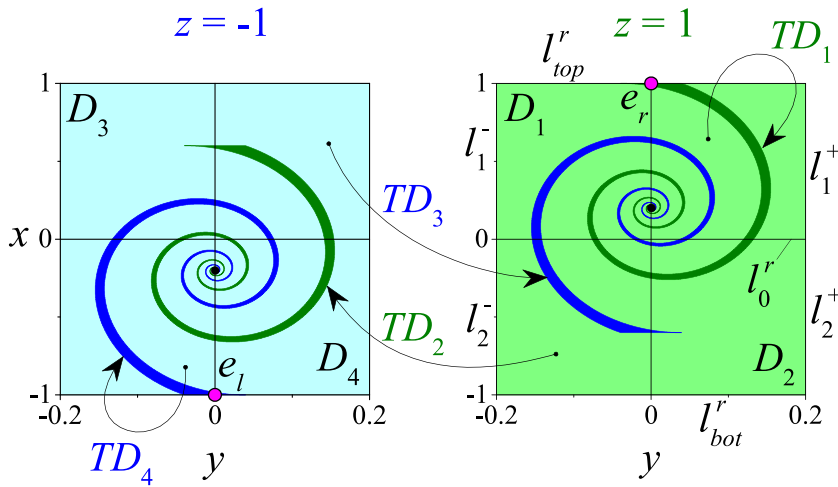


FIG. 4. The action of Poincaré return map T on the two-part cross sections $D_r = D_1 \cup D_2$ (right panel/light green) and $D_l = D_3 \cup D_4$ (left panel/light blue). Rectangles D_1 and D_2 are mapped into the spiral strips TD_1 and TD_2 , respectively (dark green). Rectangles D_3 and D_4 are mapped into the spiral strips TD_3 and TD_4 , respectively (dark blue). All spiral strips are plotted via the analytic formulas (35)–(37). Parameters $\mu = 0.2$, $\nu = 0.3$, $r = 1.02$, and $q = 0.196$ satisfy the conditions of Theorem 3. Hereafter, the variable x is scaled by the factor h due to (26).

vectors $(0, 0, -1)$ and $(0, 0, 1)$, respectively. Note that the map is always one-to-one.

In the following, we will focus on the specific range of parameter $0 < \nu < 1$, also known as the saddle index,³⁵ which can yield Shilnikov spiral chaos.³ Notice that for $1/2 \leq \nu < 1$, the Jacobian determinant (31) on the cross section D_r with $z = 1$ is

$$J = (1 - \mu)q|x|^{2\nu-1}(\nu + \omega y) < 1 \tag{32}$$

since $(1 - \mu) < 1$ and $q < 1$ due to (30), the new variable $x < 1$ due to the scaling (26), and $(\nu + \omega y) < 1$ due to the right-hand side of inequality (17c). Similarly, $|J| < 1$ on the cross-sectional domain D_l due to the symmetry. However, when $0 < \nu < 1/2$, there appears the regions in D_r and D_l :

$$D_{exp} = \{|x|^{1-2\nu} < (1 - \mu)q(\nu + \omega y), |y| < \sqrt{r^2 - 1}\}, \tag{33}$$

where $|J| > 1$ and the map (27) is expanding since the saddle-focus system A_0 expands the volume due to the divergence of its vector field $\text{div}F_{A_0} = \nabla F_{A_0} = 1 - 2\nu > 0$. As a result, attractors of map (27) cannot be located entirely in the domain D_{ext} which corresponds to small values of x . However, larger values of x from $D_r \setminus D_{exp}$ yield $J < 1$, providing the overall convergent properties of the attractors whose trajectories, in addition to the region D_{exp} , must also visit $D_r \setminus D_{exp}$.

IV. DYNAMICS OF MAP T

To prove the existence of a double-scroll attractor in the system (1) and characterize its complex structure, we seek to analyze attractors of Poincaré return map T , given in (27). To do so, we need to determine how the action of the map T transforms the cross sections D_l and D_r .

A. Spiral strips as the images of cross sections D_l and D_r .

We denote the borders of the subsections D_1 and D_2 , which form the section D_r ,

$$\begin{aligned} l_{top}^r &= (x = 1, |y| < \sqrt{r^2 - 1}, z = +1), \\ l_{bot}^r &= (x = -1, |y| < \sqrt{r^2 - 1}, z = +1), \\ l_1^+ &= (0 < x < 1, y = \sqrt{r^2 - 1}, z = +1), \\ l_1^- &= (0 < x < 1, y = -\sqrt{r^2 - 1}, z = +1), \\ l_2^+ &= (-1 < x < 0, y = \sqrt{r^2 - 1}, z = +1), \\ l_2^- &= (-1 < x < 0, y = -\sqrt{r^2 - 1}, z = +1) \end{aligned} \tag{34}$$

and the segment l_0^r separating D_1 and D_2 (Fig. 4) and given in (28). Similarly, replacing $z = 1$ with $z = -1$ in (34) and switching the superscripts r to l and subscripts $1 \rightarrow 3, 2 \rightarrow 4$, we define the corresponding borders $l_{top}^l, l_{bot}^l, l_3^+, l_3^-, l_4^+, l_4^-, l_0^l$ of the subsections D_3 and D_4 forming the section D_l .

We start by finding the first images TD_1 and TD_2 of the subsections D_1 and D_2 . *Image TD_1* : $D_1 \rightarrow D_r$. The subsection D_1 is bounded by four segments: its top l_{top}^r , bottom l_0^r , and the left and right sides, l_1^- and l_1^+ (see Fig. 4). Under the action of the map (27), all four segments are mapped into $D_r = D_1 \cup D_2$. The image of segment l_{top}^r is $\bar{l}_{top}^r = (x = 1, |y| < q\sqrt{r^2 - 1}, z = 1)$ so that the x -coordinate is preserved under the action of the map, whereas its size in y has contracted. The image of the segment l_0^r collapses to the point $M_r(\mu, 0, 1)$ as defined in (29). To construct its image, it is convenient to represent the part of subsection $D_1 \setminus (l_{top}^r \cup l_0^r)$ as a one-parameter foliation of vertical segments $l_1^r = \{0 < x < 1, y = \text{const} \in [-\sqrt{r^2 - 1}, \sqrt{r^2 - 1}], z = 1\}$, including its left and right borders, l_1^- and l_1^+ . Therefore, the image $\bar{l}_1^r = Tl_1^r$ is a one-parameter foliation of clockwise rotating spirals originating

from boundary points of \bar{l}_{top}^- and approaching their center at point M_r . These spirals are given in a parametric form,

$$\begin{aligned} \bar{x} &= \mu + (1 - \mu)x^v \sqrt{1 + y^2} \cos(\arctan y - \omega \ln x), \\ \bar{y} &= qx^v \sqrt{1 + y^2} \sin(\arctan y - \omega \ln x), \\ \bar{z} &= 1, \end{aligned} \tag{35}$$

obtained by substituting $x > 0$ and $z = 1$ into (27), multiplying and dividing the right-hand side by $\sqrt{1 + y^2}$ and using trigonometric identities

$$\begin{aligned} \frac{1}{1 + y^2} \cos \theta + \frac{y}{1 + y^2} \sin \theta &= \cos(\psi - \theta), \\ \frac{y}{1 + y^2} \cos \theta - \frac{1}{1 + y^2} \sin \theta &= \sin(\psi - \theta), \end{aligned} \tag{36}$$

where $\psi = \arctan y$ and $\theta = \omega \ln x$.

The images of the boundary segments l_1^- and l_1^+ are the spirals from (35), \bar{l}_1^- for $y = -\sqrt{r^2 - 1}$ and \bar{l}_1^+ for $y = \sqrt{r^2 - 1}$,

$$\begin{aligned} \bar{x} &= \mu + (1 - \mu)x^v r \cos(\mp \arctan \sqrt{r^2 - 1} - \omega \ln x), \\ \bar{y} &= qx^v r \sin(\mp \arctan \sqrt{r^2 - 1} - \omega \ln x), \\ \bar{z} &= 1, \end{aligned} \tag{37}$$

where the sign “−” (“+”) in “ \mp ” stands for l_1^- (l_1^+ , respectively). Thus, the image TD_1 is the spiral strip bounded by the horizontal segment \bar{l}_{top} , the point M_r , and the two spirals (37) [Fig. 4 (right panel)].

Image $TD_2 : D_2 \rightarrow D_l$. The subsection D_2 is bounded by four segments: its top l_0 , bottom l_{bot} , and the left and right sides, l_2^- and l_2^+ . The most prominent feature of mapping TD_2 is that it maps D_2 from the right cross section D_r into the left cross section D_l , thereby reflecting the two-scroll structure of the system’s (1) attractors. More precisely, by continuity, the border $l_0 \in D_r$ maps into point $M_l(-\mu, 0, -1) \in D_l$ due to (29). The image of segment l_{bot} is $\bar{l}_{bot} = (x = -2\mu + 1, |y| < q\sqrt{r^2 - 1}, z = -1)$. Similarly to (35), the images of lateral border segments l_2^+ and l_2^- are mapped into clockwise rotating spirals \bar{l}_2^\pm ,

$$\begin{aligned} \bar{x} &= -\mu + (1 - \mu)|x|^v r \cos(\pm \arctan \sqrt{r^2 - 1} - \omega \ln |x|), \\ \bar{y} &= q|x|^v r \sin(\pm \arctan \sqrt{r^2 - 1} - \omega \ln |x|), \\ \bar{z} &= -1, \end{aligned} \tag{38}$$

with the same sign convention as in (37). The spirals \bar{l}_2^+ and \bar{l}_2^- with the center at M_l bound the images of all vertical segments $l_2^\pm = \{-1 < x < 0, y = \text{const} \in [-\sqrt{r^2 - 1}, \sqrt{r^2 - 1}], z = 1\}$, which yield the spiral strip TD_2 , depicted in dark green in Fig. 4 (left panel).

Images $TD_3 : D_3 \rightarrow D_r$ and $TD_4 : D_4 \rightarrow D_l$. Due to the odd symmetry (3) of the original system (1), the mapping $TD_3 : D_3 \rightarrow D_r$ is equivalent to $TD_2 : D_2 \rightarrow D_l$, whereas $TD_4 : D_4 \rightarrow D_l$ is equivalent to $TD_1 : D_1 \rightarrow D_r$ with the change $x \rightarrow -x, y \rightarrow -y$, and $z \rightarrow -z$ in (27). Therefore, it is straightforward to obtain the equations for the images of borders of $D_3 : l_{top}^+, l_3^+, l_3^-, l_0$, similarly to

the borders of D_2 , and for the images of borders of $D_4 : l_0^-, l_{bot}^-, l_4^+, l_4^-$, similarly to the borders of D_1 . These images from two spiral strips are depicted in dark blue in Fig. 4.

B. Attractors of map T

From the above analysis, we conclude that the Poincaré return map T (27), in one iterate, transforms the global cross section D , composed of two cross sections D_l and D_r , into four spiral strips TD_1, TD_2, TD_3 , and TD_4 . As the map T is one-to-one, its subsequent iterate $T^2 D \subset TD$ so that the topological attractor of (27), $\mathcal{A} = \bigcap_{k=1}^\infty T^k D$, composed of all system’s limit sets, including the stable fixed points e_l and e_r , lies in the subsequent images of the cross sections D_l and D_r . However, depending on the system’s parameters, this iterative process can yield two distinct outcomes, corresponding to the emergence of (i) a double-scroll spiral attractor, which contains trajectories that visit all three partitions (2) of system’s (1) phase space or (ii) two disconnected one-scroll spiral attractors, separated in the phase space in regions $G_l \cup G_0$ and $G_0 \cup G_r$. In terms of the map T (27), this implies that for the double-scroll attractor to exist, the attractor must lie in all four spiral strips. That is, the subsequent images of the spiral strips are shrinking toward the attractor’s image; however, all four spiral strips persist to maintain connections between the subsections $D_{1,2,3,4}$. On the contrary, the double-scroll attractor disintegrates into two one-scroll attractors when the images of the spiral strips $T^k D_2$ and $T^k D_3$ eventually become absorbed by $T^k D_1$ and $T^k D_4$ and disappear. In this case, the subsections D_1 and D_4 become invariant under the action of the map T . This happens when the spiral strip $TD_1 \subset D_1$ ($TD_4 \subset D_4$) so that its subsequent images remain in D_1 (D_4), yielding a one-scroll attractor. Therefore, the requirement for the spiral strip TD_1 (TD_4) to belong to both D_1 and D_2 (D_3 and D_4) becomes a necessary condition for the existence of a double-scroll attractor. In terms of the system’s parameters, this condition can be formulated as follows.

Theorem 3 (Necessary condition for a double-scroll attractor’s existence): *Let the conditions (17a)–(17c), $v < 1$, and*

$$0 \leq \mu < \frac{\gamma}{1 + \gamma}, \tag{39}$$

where $\gamma = \frac{\omega r}{\sqrt{v^2 + \omega^2}} \exp(-\frac{v}{\omega}(\pi - \arctan \sqrt{r^2 - 1} - \arctan \frac{v}{\omega}))$ hold. Then, the map T has an attractor \mathcal{A}_{ds} whose points lie in all four spirals TD_1, TD_2, TD_3 , and TD_4 .

Proof. We aim to show that under the conditions of Theorem 3, the image of the subsection D_1 , the spiral strip TD_1 , belongs to both subsections D_1 and D_2 . In this way, the part of TD_1 that belongs to D_2 is further mapped into $D_l = D_3 \cup D_4$, thereby connecting the cross sections $D_r = D_1 \cup D_2$ and D_l so that trajectories of the non-trivial attractor \mathcal{A}_{ds} visit all four subsections $D_{1,2,3,4}$ and, therefore, lie in the four spiral strips.

The lower bound of spiral strip TD_1 is the image of the right border of subsection D_1 , the spiral l_1^+ . Therefore, we need to show that the minimum value of \bar{x} for l_1^+ (37) is negative so that the spiral \bar{l}_1^+ intersects the border l_0^+ with $x = 0$ and, hence, enters into D_2 . To do so, we analyze the x -equation for \bar{l}_1^+ in (37) and set $d\bar{x}/dx = 0$ to obtain the condition

$$(1 - \mu)rx^{v-1}(v \cos \varphi + \omega \sin \varphi) = 0, \tag{40}$$

where $\varphi = \arctan \sqrt{r^2 - 1} - \omega \ln x$. Similarly to (36), we transform the expression in the brackets to satisfy (40),

$$v \cos \varphi + \omega \sin \varphi = \sqrt{v^2 + \omega^2} \sin(\varphi + \Theta) = 0, \quad (41)$$

where $\Theta = \arctan \frac{v}{\omega}$. The equality (41) holds true if $\varphi = k\pi - \Theta$, where $k = 0, 1, 2, \dots$ correspond to the alternating local x -maxima and x -minima of spiral \tilde{l}_1^+ . The value $\varphi^* = \pi - \Theta$ corresponds to the absolute minimum value $\min \bar{x}$ for \tilde{l}_1^+ in (37) so that

$$\begin{aligned} \min \bar{x} = \bar{x}(\varphi^*) &= \mu + (1 - \mu)r(x^*)^v \cos(\pi - \Theta) \\ &= \mu - (1 - \mu)r(x^*)^v \frac{\omega}{\sqrt{v^2 + \omega^2}}, \quad \text{where} \end{aligned} \quad (42)$$

$$x^* = \exp \left(-\frac{1}{\omega} \left(\pi - \arctan \sqrt{r^2 - 1} - \arctan \frac{v}{\omega} \right) \right). \quad (43)$$

If $\min \bar{x} < 0$, then the lowest point of the spiral TD_1 lies below the line $x = 0$, which corresponds to the upper border of the subsection D_2, \tilde{l}_0 . Therefore, $TD_1 \cap D_2 \neq \emptyset$. Thus, setting $\min \bar{x} < 0$ in (42) and solving it for μ , we arrive at the inequality (39).

To complete the proof, we note that the conditions (17a)-(17c) are required for the cross sections D_l and D_r to be the global cross sections due to Theorem 2. \square

Theorem 3 provides necessary conditions for the existence of a double-scroll attractor confined inside the four spiral strips. Therefore, it remains to prove that this attractor has a chaotic component. To make our analysis more focused, we limit our attention to a particular choice of parameters that satisfy Theorem 3: $\mu = 0$ and $v < 1$. Recall that $\mu = 0$ corresponds to the formation of two Shilnikov homoclinic orbits to the saddle-focus O , which, due to the odd symmetry, form a figure-eight linkage. The condition $v < 1$ guarantees that there exist countably many saddle periodic orbits in a small vicinity of each (one-scroll) saddle-focus orbit in the system (1) with $\alpha = \alpha_h$ ($\mu = 0$). This property is due to the Shilnikov saddle-focus theorem³ and its extension to Filippov piecewise-smooth systems.²⁸ As discussed in Sec. III, the one-side map (27) for the global dynamics in the cross section D_l coincides with the classical Shilnikov map³⁵ for the local dynamics near a one-scroll homoclinic orbit. Hence, it is straightforward to extend Shilnikov's local analysis³⁵⁻³⁷ to the global dynamics by analytically demonstrating the existence of Smale horseshoes,³⁸ associated with a global chaotic set lying in D_l (and in D_r due to the symmetry). This analysis will serve the purpose of showing that the double-scroll attractor contains a chaotic set. In the following, we will present such a proof; however, we will also take the extra step and reveal the additional, hidden complexity of the double-scroll attractor due to the interactions of between different horseshoes and their preimages.

V. COMPLEXITY OF THE ATTRACTOR AT THE FIGURE-EIGHT HOMOCLINIC BIFURCATION

Hereafter, we consider the map (27) for $\mu = 0, v < 1$ corresponding to the Shilnikov condition.³

A. Trapping region for the double-scroll attractor

The map (27) has two stable fixed points, $e_l(x = -1, y = 0, z = -1) \in D_l$ and $e_r(x = 1, y = 0, z = 1) \in D_r$ with multipliers $s_1 = v < 1$ and $s_2 = q < 1$ (pink solid circles in Fig. 4). These two stable fixed points are the traces of two stable foci $e_{l,r}$ from the original system (1). Recall that for $\mu = 0$, which corresponds to $\alpha = \alpha_h$ in Theorem 1, the absorbing domain of system (1) is bounded by the limit cycle C_1 , depicted in Fig. 3(b). In terms of the map (27), this limit cycle corresponds to the stable period-2 orbit $o_1(x = \mp 1, y = 0, z = \pm 1)$ with multipliers $s_1 = v^2 < 1$ and $s_2 = q^2 < 1$ (Fig. 5). Thus, for the double-scroll attractor to exist, there must be saddle points/orbits whose stable manifolds separate the attractor from the stable point e_r (e_l) in D_l (D_r) and the stable period-2 orbit o_1 alternating between D_2 and D_3 . While deriving the explicit coordinates of such saddle points is not feasible, proving their existence is straightforward. The equations for finding fixed points of the map (27) with $\mu = 0$ and $z = 1$ are

$$\begin{aligned} x &= |x|^v (y \sin(\omega \ln |x|) + \cos(\omega \ln |x|)), \\ y &= q|x|^v (y \cos(\omega \ln |x|) - \sin(\omega \ln |x|)). \end{aligned} \quad (44)$$

Searching for fixed points in D_l with $x > 0$, we omit the absolute value sign in (44) to arrive at the condition

$$\begin{aligned} Q(x) &= \cos(\omega \ln x) - \frac{qx^v + x^{1-v}}{1 + qx} = 0, \\ y_s &= \frac{qx_s^v \sin(\omega \ln x_s)}{qx_s^v \cos(\omega \ln x_s) - 1}. \end{aligned} \quad (45)$$

The equation $Q(x) = 0$ has the solution $x = 1$, which corresponds to the stable fixed point e_r . The transcendental equation (45) for finding its other roots cannot be solved in a closed form. However, we can demonstrate that it has exactly one root on the interval $x \in (\tilde{x}, 1)$, where $\tilde{x} = e^{-\frac{\pi}{2\omega}}$ is chosen as a reference point that simplifies the analysis. The derivative $Q_x(1) = -(1 - v)(1 - q)/(1 + q) < 0$ as $v < 1$ and $q < 1$, and therefore, for $x = 1 - \varepsilon$ with a small $\varepsilon > 0$, the function $Q(x)$ is positive. On the other hand, the function $Q(\tilde{x}) < 0$ for $\tilde{x} = e^{-\frac{\pi}{2\omega}} < 1$. Hence, the equation $Q(x) = 0$ has the solution $x = x_s \in (\tilde{x}, 1)$, which yields the fixed point $e_{s1} = (x_s, y_s, z = 1)$. Moreover, this fixed point is unique on the interval $x \in [\tilde{x}, 1]$. Indeed, it is straightforward to show that the function $Q(x)$ changes its sign only once on the interval $(\tilde{x}, 1)$ as the derivative $Q_x(x)$ monotonically increases with decreasing x from $x = 1$ to $x = \tilde{x}$. As the fixed point e_r is a stable node with real multipliers s_1 and s_2 , the other fixed point, e_{s1} , may not be stable. Given the strong contraction along the y -coordinate in (27), the fixed point e_{s1} is a saddle with a stable manifold aligned along the y -coordinate and an unstable manifold reaching out to e_r (Fig. 5). By symmetry, there also exists its symmetrical counterpart in D_l , the saddle fixed point $e_{s2} = (-x_s, -y_s, z = -1)$.

Similarly, it is straightforward to demonstrate the existence of a period-2 saddle orbit $o_2 = (x = \mp x_s, y = \mp y_s, z = \pm 1)$ whose \mp alternating coordinates are odd-symmetric to the saddle fixed points, $e_{s1, s2}$, respectively. Indeed, it follows from the map (27) that $T(x_s, y_s, -1) = (-x_s, -y_s, 1)$. Hence, the equation for finding period-2 fixed points of (27) coincides with (45), and the same argument used for demonstrating the existence and stability of

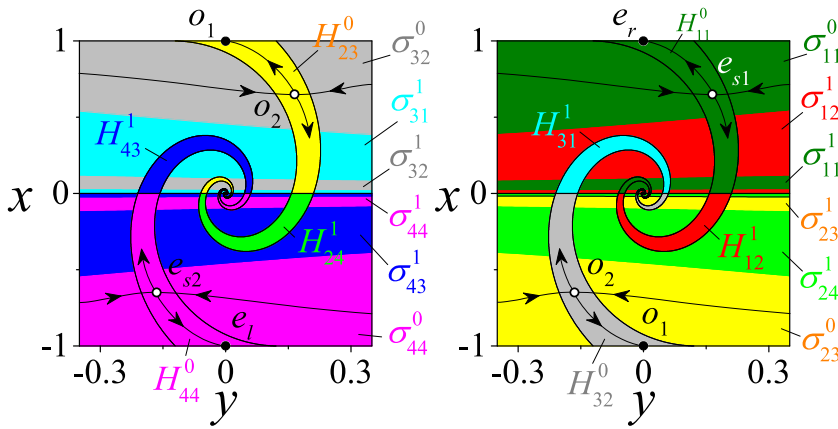


FIG. 5. Mutual arrangement of horseshoes and pre-images in cross sections D_l (left) and D_r (right) at the figure-eight homoclinic bifurcation. All images and preimages are calculated analytically via explicit formulas (37) and (38) and (50)–(55). The same color indicates the image and its own preimage. For illustrative purposes, saddle fixed points e_{s1} and e_{s2} are displaced from their actual locations $x_s = \pm 0.948$, $y_s = \pm 0.046$. Parameters: $\nu = 0.8$, $\omega = 2$, $r = 1.07$, $\mu = 0$, $q = 0.318$.

period-1 fixed points $e_{s1,s2}$ applies to o_2 . Finally, we mention that the stable invariant manifolds of saddles $e_{s1,s2}$ and period-2 saddle orbit o_2 are smooth integral curves $x = \xi_i(y)$, $|y| \leq \sqrt{r^2 - 1}$, $\xi_i \in D_i$, $i = 1, 4$, which form the trapping region $\Sigma = \Sigma_l \cup \Sigma_r$, which confines non-trivial attractors of map (27), where

$$\begin{aligned} \Sigma_r &= \left(\xi_2(x, y) < x < \xi_1(x, y), |y| \leq \sqrt{r^2 - 1}, z = 1 \right), \\ \Sigma_l &= \left(\xi_4(x, y) < x < \xi_3(x, y), |y| \leq \sqrt{r^2 - 1}, z = -1 \right). \end{aligned} \tag{46}$$

Again, writing the explicit expression for functions $\xi_{1,2,3,4}$ is out of reach. However, it is straightforward to show that in the limit of small $q \ll 1$, the stable manifolds $W_{e_{s1}}^s$ ($W_{e_{s2}}^s$) of e_{s1} (e_{s2}) are approximated by a Taylor series in q : $x = \xi_1 = x_{s1} + k_1 q(y - y_s) + \dots$, $z = 1$ ($x = \xi_2 = x_{s2} + k_2 q(y - y_s) + \dots$, $z = -1$), where $k_{1,2}$ are coefficients from the linearization about the fixed point. Similarly, the stable manifolds $W_{o_2}^s$ of period-2 saddle orbit o_2 can be approximated by $x = \xi_{3,4} = x_{s2,s1} + k_3 q(y - y_s) + \dots$, $z = \mp 1$, where k_3 is a coefficient from the linearization about o_2 . Note that for small q , the saddle fixed point e_{s1} (e_{s2}) is located very close to the stable fixed point e_1 (e_2), and its stable manifolds $W_{e_{s1}}^s$ ($W_{e_{s2}}^s$) practically coincide with the upper border of section D_r , l_{top}^r (D_l , l_{top}^l). The same claim carries over to the mutual arrangement of period-2 orbits o_1 and o_2 , whose stable manifolds $W_{e_{o2}}^s$ coincide with the lower borders of $D_{r,l}$, the lines l_{bot}^r and l_{bot}^l . Figure 5 illustrates these arrangements. Notably, even for non-small $q = 0.318$, the saddle fixed points $e_{s1,2}$ and period-2 orbit o_2 still lie quite close to their counterparts $e_{1,2}$ and o_1 . To better highlight the trapping region, we knowingly displaced the points $e_{s1,2}$ and period-2 orbit o_2 in Fig. 5 away from their actual locations. In reality, the trapping region (46) for a double-scroll attractor practically coincides with the entire sections D_r and D_l for a large set of parameters satisfying Theorem 3.

To uncover the complexity of the attractor's structure confined inside the parts of four spirals lying inside the trapping region Σ bounded by the stable manifolds of $e_{s1,2}$ and o_2 , we start bookkeeping the images and preimages of these spiral parts.

B. Images and preimages of the spiral strips

Each of the four spiral strips TD_j , $j = \overline{1, 4}$, contains two sets of infinitely many arc strips obtained by cutting the spiral strip by

the line $x = 0$ (one set for $x > 0$ and one for $x < 0$) (Fig. 4). All attractors of the map T lie in possible intersections between the spiral strips and their preimages. Overall, there are eight intersection sets

$$H_{ij} = TD_i \cap D_j, \tag{47}$$

where the permissible intersections are defined by pairs $\{ij\}$, $i, j = \overline{1, 4}$, given by the graph \mathcal{G} (Fig. 6) with the adjacency matrix,

$$G = \begin{pmatrix} 1 & 1 & 0 & 0 \\ 0 & 0 & 1 & 1 \\ 1 & 1 & 0 & 0 \\ 0 & 0 & 1 & 1 \end{pmatrix}. \tag{48}$$

For example, the sets H_{11} and H_{12} are non-empty, but the intersection set $H_{13} = TD_1 \cap D_3 = \emptyset$ since there is no edge 13 in the graph \mathcal{G} . Each permissible set $H_{ij} = \bigcup_{n=0}^{\infty} H_{ij}^n$ consists of the first stretch of the spiral strip TD_i , H_{ij}^0 , connecting $x = 0$ with $x = \pm 1$,

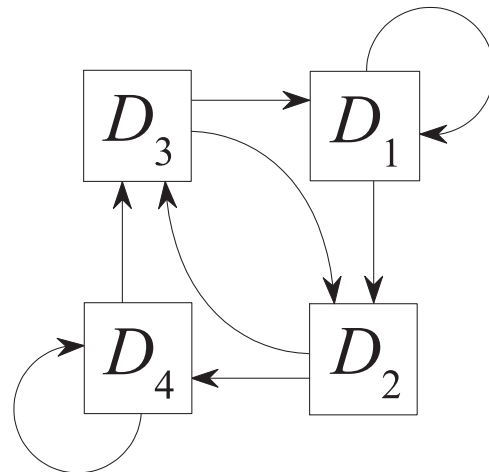


FIG. 6. Transition graph \mathcal{G} for the action of map T on four subsections $D_{1,2,3,4}$.

and the arc strips H_{ij}^n , $n = 1, 2, \dots, \infty$, where the index n corresponds to the n th scroll of spiral strip TD_i . Here, H_{ij}^1 indicates the largest arc with $n = 1$. Hereafter, we call the first stretches H_{ij}^0 and arc strips H_{ij}^n , “sleeves” and “horseshoes,” respectively. Figure 5 illustrates the mutual arrangements of the sleeves and horseshoes and justifies the terms’ choice.

We denote the preimages of the sleeves and horseshoes as

$$\sigma_{ij} = \bigcup_{n=0}^{\infty} \sigma_{ij}^n = T^{-1}H_{ij}, \quad \text{where} \quad \sigma_{ij}^n = T^{-1}H_{ij}^n.$$

For example, the union of preimages σ_{11} and σ_{12} [multiple green and red horizontal segments in Fig. 5 (right)] constitutes the section D_1 . In the following, we will characterize the essential role of the horseshoes and their preimages in the formation of a chaotic component of attractor \mathcal{A}_{ds} .

1. Preimages of H_{11} and H_{12}

Recall that the set H_{11} (lying in D_1 with $x > 0$) and H_{12} (lying in D_2 with $x < 0$) constitutes the spiral strip TD_1 . The intersection set H_{11} consists of the sleeve H_{11}^0 , emanating from the top border of D_1 , l_{top} , and ending at the lower border of D_1 , l'_0 , and the horseshoes $H_{11}^{1,2,\dots,\infty}$ starting from and ending at l'_0 with $x = 0$. Therefore, the borders of the preimages of sleeve and horseshoes, $\sigma_{11}^n = T^{-1}H_{11}^n$, $n = 0, 1, \dots, \infty$ can be found by setting $\bar{x} = 0$ in (27) with $x > 0$ and $\mu = 0$ and solving for x and y . This yields a set of level curves

$$x_k^{(1)} = \exp\left(-\frac{1}{\omega}\left(-\arctan y + \frac{\pi}{2} + \pi k\right)\right), \quad |y| < \sqrt{r^2 - 1}, \quad (49)$$

where $k = 0, 1, \dots, \infty$ is an auxiliary index to be specified differently in several expressions below, and the superscript $(\cdot)^{(1)}$ indicates the relation to section D_1 . The expression (49) is obtained by using trigonometric identities similar to (36).

The preimages $\sigma_{11} = \bigcup_{n=0}^{\infty} \sigma_{11}^n$ are an infinite set of level strips bounded by level curves (49) such that

$$\sigma_{11}^n = \{x, y \mid x_k^{(1)} < x < x_{k-1}^{(1)}, \quad |y| < \sqrt{r^2 - 1}\}, \quad (50)$$

where $k = 2n, n = 0, 1, \dots, \infty$, and $x_{-1}^{(1)} \equiv 1$ corresponds to the top border l'_{top} . These preimages are depicted by the dark green stripes in Figs. 5 and 7.

The horseshoes H_{12}^n , $n = 1, \dots, \infty$ correspond to the spiral scrolls of TD_1 in the region $x < 0$. Therefore, their preimages $\sigma_{12} = \bigcup_{n=1}^{\infty} \sigma_{12}^n$ lie between the strips σ_{11}^n and are given by the similar inequalities

$$\sigma_{12}^n = \{x, y \mid x_k^{(1)} < x < x_{k-1}^{(1)}, \quad |y| < \sqrt{r^2 - 1}\}, \quad (51)$$

where $k = 2n - 1, n = 0, 1, \dots, \infty$ (red stripes in Figs. 5 and 7).

2. Preimages of H_{23} and H_{24}

The intersection sets H_{23} and H_{24} constitute the spiral strip $TD_2 \subset (D_3 \cup D_4)$. The map (27) in D_2 takes the form

$$\begin{aligned} \bar{x} &= |x|^v (y \sin(\omega \ln |x|) + \cos(\omega \ln |x|)), \\ \bar{y} &= q|x|^v (y \cos(\omega \ln |x|) - \sin(\omega \ln |x|)), \\ \bar{z} &= -1. \end{aligned} \quad (52)$$

Therefore, the borders of preimages $\sigma_{23} = T^{-1}H_{23}$ can be calculated, similarly to (49), from the map (52) with $\bar{x} = 0$,

$$x_k^{(2)} = -x_k^{(1)}, \quad k = 0, 1, \dots, \infty. \quad (53)$$

Hence, the preimages $\sigma_{23} = \bigcup_{n=0}^{\infty} \sigma_{23}^n$ are defined as

$$\sigma_{23}^n = \{x, y \mid x_{k-1}^{(2)} < x < x_k^{(2)}, \quad |y| < \sqrt{r^2 - 1}\}, \quad (54)$$

where $k = 2n, n = 0, 1, \dots, \infty$ and $x_{-1}^{(1)} \equiv 1$ (yellow stripes in Figs. 5 and 7).

The preimages σ_{24}^n (light green stripes in Figs. 5 and 7) alternating with σ_{23}^n to fill in the entire section D_2 are given by

$$\sigma_{24}^n = \{x, y \mid x_{k-1}^{(2)} < x < x_k^{(2)}, \quad |y| < \sqrt{r^2 - 1}\}, \quad (55)$$

where $k = 2n - 1, n = 1, \dots, \infty$.

Similarly, the preimages of the intersection set H_{31} and H_{32} (H_{43} and H_{44}) forming the spiral strip TD_3 (TD_4) can be obtained from (50), (51), (54), (55) by the virtue of the symmetry (3) and the map (27). Figures 5 and 7 display the preimages σ_{31} , σ_{32} , σ_{43} , and σ_{44} , which fill in the entire section D_i (Fig. 5). In an analogous sense, this process of constructing the preimages can be viewed backward as the process of shredding a printer paper (the cross section D_1) into imperfectly shaped slices of various widths (the preimages σ_{31} , σ_{32} , σ_{43} , and σ_{44}).

C. Smale horseshoes as a classical criterion for the attractor’s complexity

Toward our goal of showing that the double-scroll attractor confined inside the trapping region has a chaotic component, we first demonstrate the existence of Smale horseshoes³⁹ that guarantee that the attractor at the figure-eight homoclinic bifurcation contains countably many saddle orbits. To do so, we need to show that the preimage σ_{11}^n (σ_{44}^n) can be transversely intersected by its image H_{11}^n (H_{44}^n). This amounts to considering the figure-eight homoclinic linkage as a combination of the Shilnikov homoclinic orbit, formed by W_1^n in the region $G_r \cup G_0$ and its symmetrical counterpart, formed by W_2^n in the region $G_l \cup G_0$ (Fig. 2). Each homoclinic orbit is associated with a separate set of Smale horseshoes that are located in either D_1 or D_4 . Thus, we follow the classical approach due to Shilnikov³⁵ to demonstrate the complexity of trajectories’ induced by each homoclinic orbit, except that our analysis relates to the global structure of the system’s limit set beyond the small neighborhood of the homoclinic orbits. The following assertion connects the existence of Smale horseshoes to the saddle index $\nu < 1$.

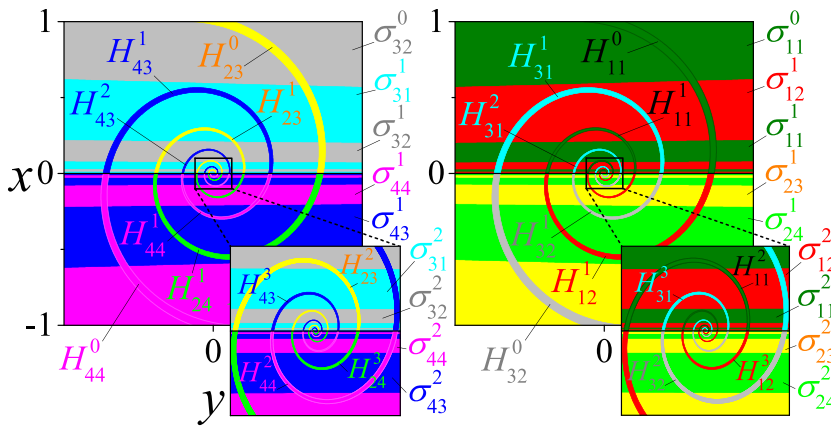


FIG. 7. Illustration of Theorem 4. All horseshoes and preimages are calculated analytically. The notations and color-coding are as in Fig. 5. The insets magnify the vicinity of the saddle-focus equilibrium. Parameters: $\nu = 0.6$, $\omega = 3$, $r = 1.01$, $\mu = 0$, $q = 0.126$.

Theorem 4 (Sufficient condition for the existence of Smale horseshoes): Under the conditions of Theorem 3, $\mu = 0$, and

$$\nu < \frac{2n_0 - 1}{2n_0}, \quad n_0 \geq 1, \tag{56}$$

the nonlocal trapping region Σ contains an infinite number of Smale horseshoes $H_{11}^n \cap \sigma_{11}^n$ ($H_{44}^n \cap \sigma_{44}^n$) for $n = n_0, n_0 + 1, n_0 + 2, \dots$

Proof. Theorem 3 guarantees that the double-scroll attractor lies in the four spiral strips. The condition $\mu = 0$ implies the existence of the figure-eight homoclinic linkage in the system (1). To prove the claim of Theorem 4, it is sufficient to derive the conditions under which the horseshoe H_{11}^n transversely intersects its image σ_{11}^n . This is true if the maximum point of the lower bound of H_{11}^n lies above the top border of the preimage σ_{11}^n (for example, compare the mutual arrangement of H_{11}^1 and σ_{11}^1 in Fig. 7). To demonstrate this property, we first calculate extreme points of the horseshoes H_{11}^n whose boundaries are given by the upper arcs of the spirals \bar{l}_1^- and \bar{l}_1^+ (37). To do so, similarly to the proof of Theorem 3, we set $d\bar{x}/dx = 0$ in (37) to obtain the condition (41) with $\varphi = \mp \arctan \sqrt{r^2 - 1} - \omega \ln x$ and $\Theta = \mp \arctan \frac{\nu}{\omega}$. Hereafter, “−” (“+”) in “ \mp ” corresponds to \bar{l}_1^- (\bar{l}_1^+). Therefore, the local x -minima and x -maxima are reached at the points,

$$x = x_k^{-(+)} = \exp\left(\frac{1}{\omega} \left(-\pi k + \arctan \frac{\nu}{\omega} \mp \arctan \sqrt{r^2 - 1}\right)\right), \tag{57}$$

where $k = 1, 2, \dots$. Hence, the corresponding local x -minima and x -maxima are

$$\bar{x}(x_k^{-(+)}) = (-1)^k \frac{r\omega}{\sqrt{\nu^2 + \omega^2}} (x_k^{-(+)})^\nu, \quad k = 1, 2, \dots \tag{58}$$

Comparing the values in (58), we conclude that the lower maximum point of the n th horseshoe H_{11}^n is

$$\begin{aligned} x_{\max}^- &= \frac{r\omega}{\sqrt{\nu^2 + \omega^2}} (x_{2n}^-)^\nu, \\ y_{\max}^- &= -q \frac{r\nu}{\sqrt{\nu^2 + \omega^2}} (x_{2n}^-)^\nu, \quad n = 1, 2, \dots \end{aligned} \tag{59}$$

If this point lies higher than the top boundary of preimage σ_{11}^n given by the equation

$$x_{2n-1}^{(1)} = \exp\left(\frac{1}{\omega} \left(\arctan y - \frac{\pi}{2} - \pi(2n - 1)\right)\right) \tag{60}$$

with $|y| \leq \sqrt{r^2 - 1}$, then σ_{11}^n and H_{11}^n form the Smale horseshoe Sh_n^{11} . Thus, we obtain sufficient conditions for the existence of the Smale horseshoe Sh_n^{11} ,

$$\frac{r\omega}{\sqrt{\nu^2 + \omega^2}} (x_{2n}^-)^\nu > \exp\left(\frac{1}{\omega} \left(\arctan y_{\max}^- - \frac{\pi}{2} - \pi(2n - 1)\right)\right). \tag{61}$$

This inequality further transforms into

$$R > e^{\frac{1}{\omega} (\arctan \sqrt{r^2 - 1} - \frac{\pi}{2} - \arctan |y_{\max}^-| - 2\pi n (\frac{2n-1}{2n} - \nu))}, \tag{62}$$

where $R = \frac{r}{\sqrt{1+(\frac{\nu}{\omega})^2}} \exp\left(\frac{\nu}{\omega} \arctan \frac{\nu}{\omega}\right)$. Since $r > 1$ and $\frac{1}{\sqrt{1+(\frac{\nu}{\omega})^2}} e^{\frac{\nu}{\omega} \arctan \frac{\nu}{\omega}} > 1$ for any $\frac{\nu}{\omega} > 0$, we conclude that $R > 1$. Therefore, under the condition (56), the power of the exponent on the right-hand side of inequality (62) is negative for $n = n_0$. Thus, the inequality is valid for any $n = n_0, n_0 + 1, n_0 + 2, \dots$, as the function $\frac{2n-1}{2n}$ increases. Due to the symmetry, the same proof and the condition (56) apply to the Smale horseshoe $H_{44}^n \cap \sigma_{44}^n$. \square

Remark 2: The condition (56) gives the order in which horseshoes H_{11}^n (H_{44}^n) turn into Smale horseshoes, thereby suggesting that the limit set of trajectories becomes more complex by decreasing the saddle index $\nu < 1$. This set reaches its maximum complexity when $\nu < 1/2$ so that all horseshoes H_{11}^n (H_{44}^n), $n = 1, 2, \dots$ generate Smale horseshoes. Note that each Smale horseshoe induces a set of countably many saddle periodic orbits whose symbolic representation has an alphabet of the Bernoulli shift consisting of two symbols.³⁹

Thus, collecting the statements of Theorems 1–4, we conclude that the system (1) has a global double-scroll attractor with a chaotic component determined by an infinite number of Smale horseshoes. In the following, we will show that the attractor’s structure also contains an additional, hidden set of saddle periodic trajectories due to multi-periodic interactions between the horseshoes.

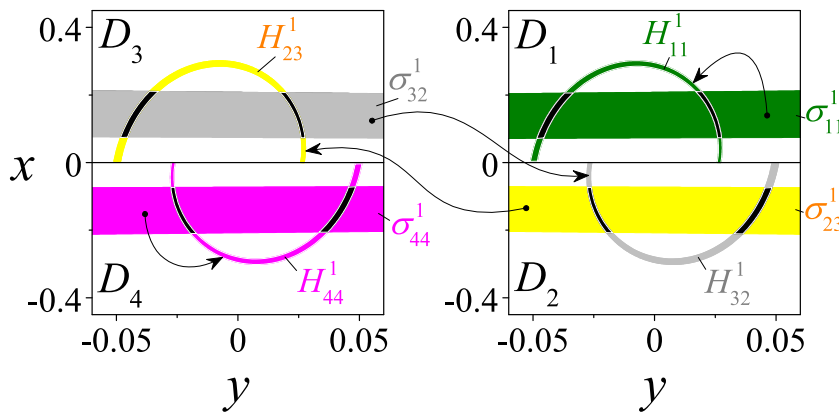


FIG. 8. The classical Smale horseshoes $\sigma_{11}^1 \rightarrow \sigma_{11}^1$ (green) and $\sigma_{44}^1 \rightarrow \sigma_{44}^1$ (purple) co-exist with the period-two Smale horseshoe $\sigma_{32}^1 \rightarrow \sigma_{23}^1 \rightarrow \sigma_{32}^1$ (the combination of the gray and yellow arcs and strips). The black areas display the intersections of the images and preimages. All horseshoes and their preimages are calculated analytically via explicit formulas (37)–(38) and (50)–(55). Parameters are as in Fig. 7.

D. The hidden complexity of the double-scroll attractor

So far, we have concentrated on the classical Smale horseshoes whose initial formation requires one iterate of map (27) that makes the horseshoe H_{11}^n transversely intersect its own preimage σ_{11}^n . Obviously, the intersection of a horseshoe with its own preimage is required to yield an infinite set of saddle periodic orbits. However, this formation may take more than one iterate, yielding a *multi-period* Smale horseshoe, where the period indicates the number of iterates required to complete the loop and return the horseshoe back to the preimage. We will first explain the formation of a period-two Smale horseshoe in the section D_3 and then make general statements on the emergence of multi-period and *infinite-period* Smale horseshoes.

For illustrative purposes, we begin with the preimage $\sigma_{32}^1 \subset D_3$ and its image, horseshoe $H_{32}^1 \subset D_2$ (Fig. 8), which intersects the preimage $\sigma_{23}^1 \subset D_2$. In turn, the horseshoe $H_{23}^1 \subset D_3$ and intersects the preimage σ_{32}^1 . Assume that these intersections are transversal (we will formalize this assumption later in this subsection). Thus, in two iterates, this sequence leads to the formation of the period-two Smale horseshoe $Sh_2^1 = \sigma_{32}^1 \rightarrow \sigma_{23}^1 \rightarrow \sigma_{32}^1$. The non-wandering hyperbolic set associated with the period-two Smale horseshoe Sh_2^1 lies in four regions $(\sigma_{32}^1 \cap H_{23}^1) \cup (\sigma_{23}^1 \cap H_{32}^1)$ and, therefore, is

topologically conjugate to the Bernoulli shift on four symbols. Note that this alphabet of $2p$ symbols differs from the two-symbol alphabet of the classical Smale horse by a factor of period $p = 2$. Figure 8 displays the formation of this period-two Smale horseshoe. It is convenient to view this formation process as a period-two chain of interacting horseshoes. In terms of the transition graph \mathcal{G} (48) with vertices (1, 2, 3, 4) corresponding to the sections D_1, D_2, D_3, D_4 , this period-two chain inducing Sh_2^1 can be represented by an infinite length sequence 323232...

This argument applies to the full set of period-two Smale horseshoes $Sh_2^n = \sigma_{32}^n \rightarrow \sigma_{23}^n \rightarrow \sigma_{32}^n$ for $n = 1, 2, \dots$. As the formation of a Smale horseshoe, which yields a hyperbolic limit set of trajectories, requires transversal intersections between the preimages and images, we will call such Smale horseshoes *hyperbolic*. Otherwise, we will refer to the chains of interacting horseshoes with non-transversal intersections as *elliptic*. Such elliptic chains generate stable periodic orbits. The following assertion gives the condition for the Smale horseshoes Sh_2^n to be hyperbolic.

Theorem 5: *Let the condition (56) hold. Then, there exist an infinite number of period-two hyperbolic Smale horseshoes $Sh_2^n = \sigma_{32}^n \rightarrow \sigma_{23}^n \rightarrow \sigma_{32}^n$ with $n = n_0, n_0 + 1, n_0 + 2, \dots$*

Proof. This simple assertion can be proven similarly to Theorem 4. It is sufficient to show that if the lower maximum point of the n th horseshoe H_{23}^n lies above the upper border of preimage

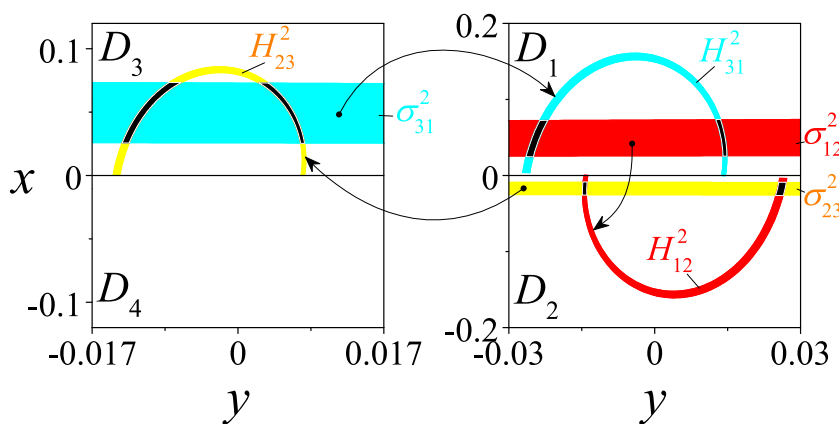


FIG. 9. Period-three Smale horseshoe. The arrow lines indicate the transition chain of preimages $\sigma_{31}^2 \rightarrow \sigma_{12}^2 \rightarrow \sigma_{23}^2 \rightarrow \sigma_{31}^2$. Parameters are as in Fig. 7.

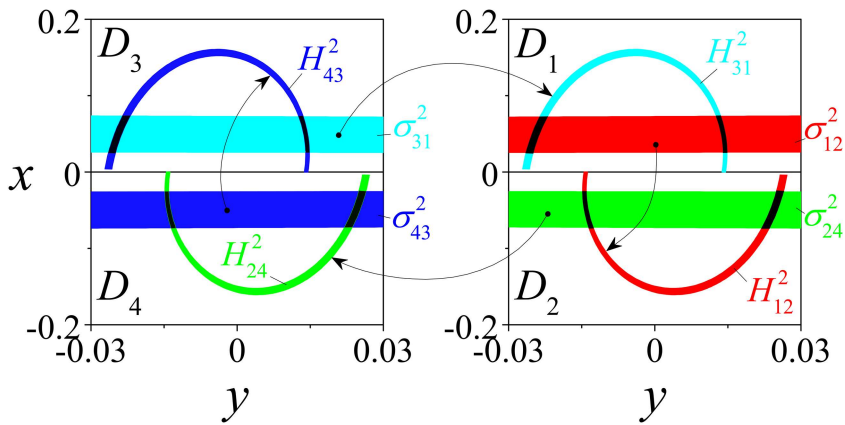


FIG. 10. Period-four Smale horseshoe $\sigma_{31}^2 \rightarrow \sigma_{12}^2 \rightarrow \sigma_{24}^2 \rightarrow \sigma_{43}^2 \rightarrow \sigma_{31}^2$. The notations and parameters are as in Fig. 8.

σ_{32}^n (Fig. 8), then $\sigma_{32}^n, \sigma_{23}^n, H_{23}^n$, and H_{32}^n yield transversal intersections and form a period-two hyperbolic Smale horseshoe. Due to the symmetry, the equations for the coordinates of the maximum point and the upper border, respectively, coincide with (59) and (60), subject to the sign change in y . Therefore, the inequality (56) guarantees the transversal intersections. \square

Remarkably, the action of the map T can induce multi-period Smale horseshoes, which may involve interactions between the horseshoes from different sections as in the example above or interactions within one section (D_1 or D_4). In the latter case, such multi-period Smale horseshoes are induced by a one-scroll Shilnikov homoclinic orbit. In general, a hyperbolic period- p Smale horseshoe Sh_p^n corresponds to the transition chain of preimages: $\sigma_{i_1 j_1}^n$

$\rightarrow \sigma_{i_2 j_2}^n \rightarrow \dots \rightarrow \sigma_{i_p j_p}^n \rightarrow \sigma_{i_{p+1} j_{p+1}}^n = \sigma_{i_1 j_1}^n$, where $i_{l+1} = j_l$, such that the image $H_{i_l j_l} = T\sigma_{i_{l+1} j_{l+1}}$ of each element $\sigma_{i_{l+1} j_{l+1}}$ of the chain transversely intersects the subsequent element $\sigma_{i_l j_l}$ so that

$$H_{i_l j_l} \cap \sigma_{i_{l+1} j_{l+1}} \neq \emptyset, l = \overline{1, p}. \tag{63}$$

The limit set of the trajectories generated by the period- p Smale horseshoe is the Cantor set located in the intersections (63) with the topological alphabet with $2p$ symbols. The following theorem gives the conditions for the intersections (63) to be transversal.

Theorem 6 (Sufficient conditions for the formation of hyperbolic multi-period Smale horseshoes): Let the conditions of Theorem 3, $\mu = 0$, and

$$v < \frac{2n-1}{2m}, \quad n = 1, 2, \dots, \tag{64}$$

where $m = n + k, k \geq 1$ hold. Then, for each n ,

- A. The preimage σ_{11}^n transversely intersects k horseshoes $H_{11}^{n+i} : \sigma_{11}^n \cap (\bigcup_{i=1}^k H_{11}^{n+i})$, where the index $i = 1, \dots, k$ represents the ordering due to the decreasing size of the horseshoes compared to H_{11}^n .
- B. The preimage σ_{44}^n transversely intersects k horseshoes $H_{44}^{n+i} : \sigma_{11}^n \cap (\bigcup_{i=1}^k H_{11}^{n+i})$.
- C. The preimage σ_{23}^n transversely intersects k horseshoes $H_{32}^{n+i} : \sigma_{23}^n \cap (\bigcup_{i=1}^k H_{32}^{n+i})$.
- D. The preimage σ_{32}^n transversely intersects k horseshoes $H_{23}^{n+i} : \sigma_{32}^n \cap (\bigcup_{i=1}^k H_{23}^{n+i})$.

Proof. The proof of Claim A is similar to that of Theorem 4. We need to show the maximum point of the lower bound of the m th horseshoe H_{11}^m with the coordinates [see (59)],

$$\begin{aligned} x_{\max}^j &= \frac{r\omega}{\sqrt{v^2 + \omega^2}} (x_{2m}^j)^v, \\ y_{\max}^j &= -q \frac{rv}{\sqrt{v^2 + \omega^2}} (x_{2m}^j)^v, \end{aligned} \quad m = n + k, \quad n = 1, 2, \dots, \tag{65}$$

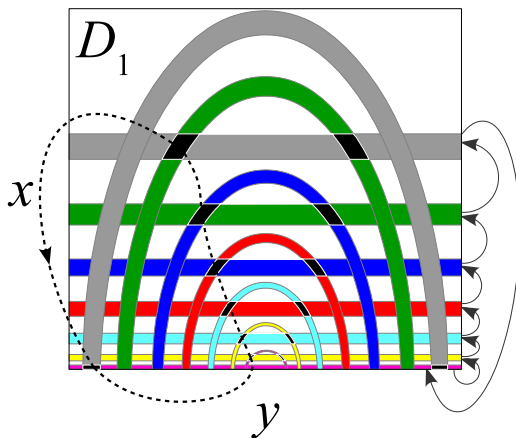


FIG. 11. Schematic representation of a period-seven Smale horseshoe formed within D_1 . The same color indicates horseshoe H_{11}^i and its image σ_{11}^i (not labeled). The solid arrow curve corresponds to the chain $\sigma_{11}^7 \rightarrow \sigma_{11}^6 \rightarrow \dots \rightarrow \sigma_{11}^1 \rightarrow \sigma_{11}^7$. Each solid arrow indicates that the initial image σ_{11}^i becomes connected to the image σ_{11}^j by the horseshoe H_{11}^i (note the color labeling). The dashed curve displays the transition of the intersection sets (black) along the chain. For example, the red strip generates the red horseshoe, which intersects the blue strip, which in turn generates the blue horseshoe so that this process becomes cyclic.

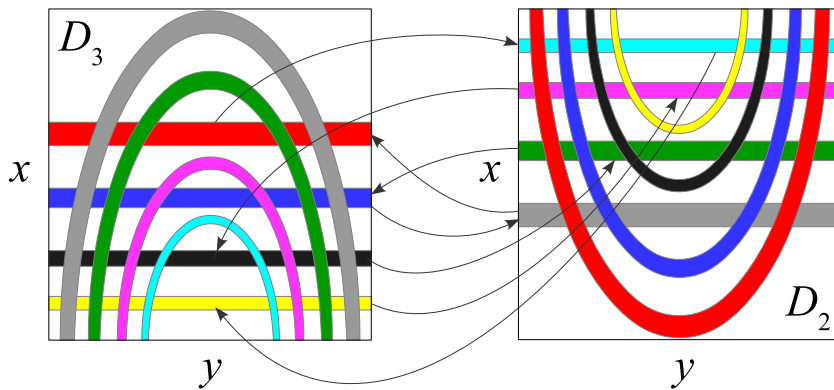


FIG. 12. Schematic representation of a period-eight Smale horseshoe formed by the transitions between sections D_2 and D_3 . The notations are as in Fig. 11. The reader is invited to follow the arrows to detect the formation of the period-eight Smale horseshoe, similar to Fig. 11. Due to the cyclic structure, the choice of the initial preimage (strip) is arbitrary.

lies above the top border of the preimage σ_{11}^n [see (60)]. This results in the inequality

$$R > e^{\frac{1}{\omega}(\nu \arctan \sqrt{r^2-1} - \frac{\pi}{2} - \arctan |y_{\max}^j| - \pi(2n-1) + 2m\nu\pi)}, \quad (66)$$

where R is defined in (62). Under the condition (64), the power of the exponent on the right-hand side of inequality (62) is negative, and since $R > 1$, the condition (66) holds true. This concludes the proof of Claim A. Due to the symmetry (3) preserving the sizes and mutual arrangements on the corresponding preimages and horseshoes, Claim A implies Claims B–D. \square

Theorem 6 highlights the crucial role of the saddle index ν in inducing multi-period Smale horseshoes. It follows from (64) that decreasing ν increases the number of intersections k , thereby connecting more horseshoes and inducing hyperbolic multi-period Smale horseshoes. For example, $n = \frac{2k\nu+1}{2(1-\nu)}$ with $k = 1$ corresponds to the index of the preimage σ_{11}^n , which becomes connected to its neighbor σ_{11}^{n+1} (via the horseshoe H_{11}^{n+1}). Note that for $\nu < \frac{1}{4}$, the condition (64) with $k = 1$ gives $n > 1$, indicating that each preimage σ_{11}^n , including the preimage σ_{11}^1 of the largest horseshoe H_{11}^1 , is connected to its neighboring preimage σ_{11}^1 . As a result, there emerges the hyperbolic period-two Smale horseshoe $Sh_2^1 = \sigma_{11}^1 \rightarrow \sigma_{11}^2 \rightarrow \sigma_{11}^1$, which corresponds to a limit set of trajectories lying far away from the neighborhood of the Shilnikov homoclinic orbit. In accordance with (64), increasing k prevents the participation of some large preimages (with small superscript indexes) in the formation of

multi-period hyperbolic horseshoes; however, it significantly promotes the overall connectivity among the other smaller preimages and potentially leads to the emergence of hyperbolic infinite-period Smale horseshoes with $p \rightarrow \infty$. In accordance with Theorem 6, this argument also applies to the emergence of period- p Smale horseshoes from interactions between preimages from different cross sections.

Figure 8 demonstrates that in addition to the classical hyperbolic set of (period-one) Smale horseshoes $Sh_n^1 : \sigma_{11}^n \rightarrow \sigma_{11}^n$ defined by Theorem 4, there exists a somewhat hidden hyperbolic set represented by period-two Smale horseshoes $Sh_2^n : \sigma_{32}^n \rightarrow \sigma_{23}^n \rightarrow \sigma_{32}^n$. Examples of higher period- p Smale horseshoes, which always coexist with infinitely many classical (period-one) Smale horseshoes, are depicted in Fig. 9 (for $Sh_3^2 : \sigma_{12}^2 \rightarrow \sigma_{23}^2 \rightarrow \sigma_{31}^2 \rightarrow \sigma_{12}^2$ with $p = 3$) and Fig. 10 (for $Sh_4^2 : \sigma_{12}^2 \rightarrow \sigma_{24}^2 \rightarrow \sigma_{43}^2 \rightarrow \sigma_{31}^2 \rightarrow \sigma_{12}^2$ with $p = 4$). Note that the period-four Smale horseshoe of Fig. 10 connects four horseshoes from all sections $D_{1,2,3,4}$ so that the saddle orbits associated with this period-four Smale horseshoe visit all four sections $D_{1,2,3,4}$ in the ascending order. Obviously, for $p \geq 5$, this order cannot be respected, and the trajectory stays in D_1 or D_4 at least twice in a row.

Figure 11 schematically illustrates the formation of period- p Smale horseshoes $Sh_p^{\text{mix}} = (\sigma_{11}^n \rightarrow \sigma_{11}^{n+p-1} \rightarrow \sigma_{11}^{n+p-2} \rightarrow \dots \rightarrow \sigma_{11}^{n+1} \rightarrow \sigma_{11}^n)$ with $p = 7$ on the cross section D_1 . Note that all (infinitely many) intersections of the horseshoes and preimages are involved in other chains of various periods. The set of these

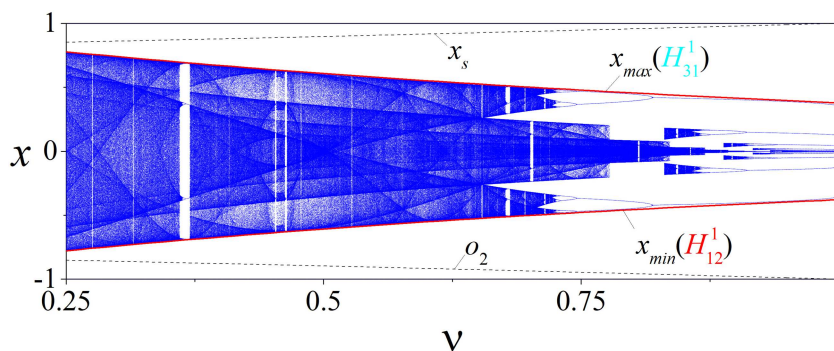


FIG. 13. The role of saddle index ν in enriching the complexity of the double-scroll attractor. The bifurcation diagram of map (27) calculated numerically from 2000 initial conditions uniformly chosen for each value ν from $x \in [-1, 1]$ with $y = 0$. The red solid curves $x_{\max}(H_{31}^1)$ and $x_{\min}(H_{12}^1)$ trace the x -maximum value of horseshoe H_{31}^1 and the x -minimum value of horseshoe H_{12}^1 . The curves are calculated analytically via $x_{\max} = \frac{r\omega}{\sqrt{\nu^2+\omega^2}} e^{-\frac{\nu}{\omega}(\pi - \arctan \sqrt{r^2-1} - \arctan \frac{x}{\omega})}$ and $x_{\min} = -x_{\max}$. The dashed black curves display the x -coordinates of saddle fixed point x_s and saddle period-two orbit o_2 . Parameters are $\mu = 0$ (corresponding to the figure-eight homoclinic orbit), $\omega = 3$, $q \approx 0$ due to $\beta = 160$.

chains essentially complements the classical set of Smale horseshoes $Sh_1^n = (\sigma_{11}^n \rightarrow \sigma_{11}^n)$. Finally, Fig. 12 displays the formation process of a period-eight Smale horseshoe, which involves the interactions between cross sections D_3 and D_2 and associated with the following transition chain:

$$Sh_8^{14321} : \begin{array}{ccccccc} \sigma_{32}^1 & \rightarrow & \sigma_{23}^4 & \rightarrow & \sigma_{32}^4 & \rightarrow & \sigma_{23}^3 \rightarrow \\ & & \rightarrow & & \sigma_{32}^3 & \rightarrow & \sigma_{23}^2 \rightarrow \\ & & & & \sigma_{32}^2 & \rightarrow & \sigma_{23}^1 \rightarrow \sigma_{32}^1. \end{array}$$

Notably, the addition of pairs $\sigma_{23}^i \rightarrow \sigma_{32}^i$, $i = 5, 6, \dots$ can lead to an infinite series of period- p Smale horseshoes with $p = 2i$, which become infinite-period Smale horseshoes in the limit of $p \rightarrow \infty$. Note that this induces a hyperbolic set with an infinite symbol topological alphabet.

In addition to the complexity associated with infinitely many transversal period- p Smale horseshoes, there always exist non-transversal intersections between some horseshoes and preimages, thereby inducing the elliptic chains of preimages. Such chain contain elements that correspond to tangencies between the stable and unstable invariant manifolds of saddle orbits, which induce stable orbits with a small basin of attractors, corresponding to Newhouse regions.^{40,41} The presence of these stable orbits makes the double-scroll attractor a quasi-strange attractor, often called a “quasiattractor.”³⁵ Figure 13 displays a bifurcation transition in the map (27) as a function of the saddle index ν . It indicates the emergence of alternating chaotic and periodic windows typical for chaotic double-scroll attractors. Remarkably, Fig. 13 provides evidence of the increasing contribution of multi-period Smale horseshoes into strengthening the chaotic component of the double-scroll attractor with decreasing saddle index ν . Indeed, in accordance with Theorem 6, decreasing saddle index ν increases the connectivity of the horseshoes, thereby generating multi-period Smale horseshoes with smaller indexes n corresponding to saddle trajectories visiting the entire trapping region of the attractor (note the increased attractor’s size at $\nu = 0.25$).

To further emphasize the complexity of the hidden chaotic set associated with multi-period and infinite-period Smale horseshoes contained inside the double-scroll attractor, we point the reader to the following statement. For any infinite one-sided sequence of vertices (1, 2, 3, 4) generated by graph \mathcal{G} and governing the transition between cross sections $D_{1,2,3,4}$, there exists at least one hyperbolic infinite-period Smale horseshoe for sufficiently small ν chosen in accordance with Theorem 6. The complexity of the underlying Cantor set can be illustrated by an example of an infinite-period chain, which corresponds to a randomly chosen infinite sequence 23111124444323231 . . . , subject to the graph \mathcal{G} . Remarkably, the cardinality of the hyperbolic set of such sequences is a continuum.

VI. CONCLUSIONS

In this paper, we gave constructive proof for the existence of a quasi-strange double-scroll attractor in a piecewise-smooth ODE system with explicit solutions. We derived a flow-defined Poincaré map for all trajectories inside the system’s absorbing domain and analyzed the complexity of the double-scroll attractor at the figure-eight Shilnikov homoclinic bifurcation. We discovered that the double-scroll attractor contains a chaotic component that is determined by multi-period or even infinite-period chains

of intersections between different horseshoes and their preimages, generated by the action of the map on two Poincaré cross sections. By the analogy with the classical Smale horseshoe that is formed by the intersection of a horseshoe with its own preimage in one iterate of the map, we referred to these iterative chains that return the preimage back to itself in several iterates as multi-period Smale horseshoes. We derived the conditions under which a given multi-period Smale horseshoe is transversal and, therefore, yields countably many saddle periodic orbits. These conditions connect the size and order of multi-period Smale horseshoes with the saddle index. They provide an ordering in which decreasing the saddle index induces additional long-period Smale horseshoes. Remarkably, a sufficiently small saddle index leads to the emergence of infinite-period Smale horseshoes, which contribute to the hidden complexity of the double-scroll attractor. Given a countable set of infinite-period Smale horseshoes, there always exist elliptic chains of preimages that contain at least one non-transversal intersection between a horseshoe and a preimage, thereby inducing weakly stable non-periodic orbits and making the double-scroll attractor a “quasi-attractor.”

The destruction of the figure-eight homoclinic orbit under the change of parameter μ decreases the number of multi-period Smale horseshoes and, therefore, decreases the complexity of the double-scroll attractor up to its split into two spiral attractors at the critical value of μ given in Theorem 3. The detailed analysis of this transition is a subject of future study.

As the double-scroll attractor of our piecewise-smooth system shares the main properties of its smooth counterparts, our analysis may suggest that the global structure of the classical Chua attractor and other figure-eight attractors might be more complex than previously thought. Our approach can also be extended to analyze the structure of multi-scroll attractors whose hidden complexity defined by infinite-period Smale horseshoes is expected to be enhanced by the multi-scroll interactions. Such multi-scroll attractors can be created by duplicating the double-scroll attractor and shifting it along the line connecting the stable focus equilibria, e_l and e_r . This process results in the stable focus e_l taking the place of e_r , while the stable focus e_r at a further shift produces an additional scroll, generating a three-scroll attractor. Continuing this duplication process can create an analytically tractable piecewise-smooth system with a saddle-focus chaotic attractor with any number of scrolls.

In this work, we concentrated on uncovering the double scroll’s hidden complexity rather than synthesizing a hidden attractor. However, it is worth noting that the saddle-focus attractor in our piecewise-smooth system co-exists with two stable focus equilibria e_l and e_r and may also be viewed as a hidden attractor as it is separated from the fixed points by the saddle limit cycles. Our approach to synthesizing piecewise-smooth dynamical systems with prescribed chaotic dynamics can be used to design various hidden chaotic attractors. These may include hidden attractors without equilibrium points,⁴² although constructing a trapping region for such systems is challenging.

ACKNOWLEDGMENTS

This work was supported by the Ministry of Science and Higher Education of the Russian Federation under Grant No.

0729-2020-0036, by the Russian Science Foundation under Grant Nos. 22-21-00553 (to V.N.B. and N.V.B) and 22-12-00348 (numerics, to N.V.B.), and by the National Science Foundation (USA) under Grant Nos. CMMI-2009329 and DMS-1909924 (to I.B.).

AUTHOR DECLARATIONS

Conflict of Interest

The authors have no conflicts to disclose.

Author Contributions

Vladimir N. Belykh: Conceptualization (lead); Formal analysis (equal); Investigation (equal); Writing – original draft (equal); Writing – review & editing (equal). **Nikita V. Barabash:** Conceptualization (equal); Formal analysis (equal); Investigation (equal); Writing – review & editing (equal). **Igor Belykh:** Conceptualization (equal); Formal analysis (equal); Investigation (equal); Writing – original draft (equal); Writing – review & editing (equal).

DATA AVAILABILITY

The data that support the findings of this study are available from the corresponding author upon reasonable request.

REFERENCES

- ¹L. Chua, M. Komuro, and T. Matsumoto, *IEEE Trans. Circuits Syst.* **33**, 1072 (1986).
- ²A. Arneodo, P. Coulet, and C. Tresser, *Commun. Math. Phys.* **79**, 573 (1981).
- ³L. P. Shilnikov, *Dokl. Akad. Nauk* **160**, 558 (1965).
- ⁴T. Matsumoto, L. Chua, and M. Komoro, *Physica D* **24**, 97 (1987).
- ⁵T. Matsumoto, L. O. Chua, and K. Ayaki, *IEEE Trans. Circuits Syst.* **35**, 909 (1988).
- ⁶V. N. Belykh and L. O. Chua, *Int. J. Bifurcat. Chaos* **2**, 697 (1992).
- ⁷R. N. Madan, *Chua's Circuit: A Paradigm for Chaos* (World Scientific Publishing, 1993).
- ⁸A. I. Khibnik, D. Roose, and L. O. Chua, *Int. J. Bifurcat. Chaos* **3**, 363 (1993).
- ⁹A. R. Champneys and Y. A. Kuznetsov, *Int. J. Bifurcat. Chaos* **4**, 785 (1994).
- ¹⁰S. Boughaba and R. Lozi, *Int. J. Bifurcat. Chaos* **10**, 205 (2000).
- ¹¹R. Lozi and S. Ushiki, *Int. J. Bifurcat. Chaos* **3**, 333 (1993).
- ¹²T. Xing, K. Pusuluri, and A. L. Shilnikov, *Chaos* **31**, 073143 (2021).
- ¹³G. A. Leonov and N. V. Kuznetsov, *Int. J. Bifurcat. Chaos* **23**, 1330002 (2013).
- ¹⁴Z. Galias and W. Tucker, *J. Differ. Equ.* **266**, 2408 (2019).
- ¹⁵L. O. Chua, *Scholarpedia* **2**, 1488 (2007).
- ¹⁶Y. A. Kuznetsov, S. Rinaldi, and A. Gragnani, *Int. J. Bifurcat. Chaos* **13**, 2157 (2003).
- ¹⁷M. Di Bernardo and S. Hogan, *Philos. Trans. R. Soc. A: Math. Phys. Eng. Sci.* **368**, 4915 (2010).
- ¹⁸D. Simpson, *Phys. Lett. A* **382**, 2439 (2018).
- ¹⁹P. Glendinning, *Eur. J. Appl. Math.* **29**, 757 (2018).
- ²⁰V. N. Belykh, N. V. Barabash, and I. V. Belykh, *Chaos* **31**, 043117 (2021).
- ²¹M. Di Bernardo, C. J. Budd, A. R. Champneys, P. Kowalczyk, A. B. Nordmark, G. O. Tost, and P. T. Piiroinen, *SIAM Rev.* **50**, 629 (2008).
- ²²A. C. Luo, *Commun. Nonlinear Sci. Numer. Simul.* **1**, 1 (2005).
- ²³A. C. Luo and B. Xue, *Int. J. Bifurcat. Chaos* **19**, 2165 (2009).
- ²⁴D. J. Simpson, S. J. Hogan, and R. Kuske, *SIAM J. Appl. Dyn. Syst.* **12**, 533 (2013).
- ²⁵M. Di Bernardo, C. Budd, A. Champneys, and P. Kowalczyk, *Piecewise-Smooth Dynamical Systems. Theory and Applications* (Springer-Verlag, New York, 2008).
- ²⁶I. Belykh, R. Kuske, M. Porfiri, and D. J. Simpson, *Chaos* **33**, 010402 (2023).
- ²⁷K. Lu, Q. Yang, and G. Chen, *Chaos* **29**, 043124 (2019).
- ²⁸D. D. Novaes and M. A. Teixeira, *Chaos* **29**, 063110 (2019).
- ²⁹J. G. Barajas-Ramírez, A. Franco-López, and H. G. González-Hernández, *Appl. Math. Comput.* **395**, 125877 (2021).
- ³⁰S. Guo and A. C. Luo, *Chaos* **32**, 033132 (2022).
- ³¹V. N. Belykh, N. V. Barabash, and I. V. Belykh, *Chaos* **29**, 103108 (2019).
- ³²G. Leonov, N. Kuznetsov, and V. Vagaitsev, *Phys. D: Nonlinear Phenom.* **241**, 1482 (2012).
- ³³M. Jeffrey, *Hidden Dynamics. The Mathematics of Switches, Decisions and Other Discontinuous Behaviour* (Springer, New York, 2018).
- ³⁴L. P. Shilnikov and A. Shilnikov, *Scholarpedia* **2**, 1891 (2007).
- ³⁵L. P. Shilnikov, A. L. Shilnikov, D. V. Turaev, and L. Chua, *Qualitative Theory in Nonlinear Dynamics. Part II* (World Scientific, 2001).
- ³⁶I. M. Ovsyannikov and L. P. Shilnikov, *Mat. Sb.* **172**, 552 (1986).
- ³⁷I. Ovsyannikov and L. Shilnikov, *Math. USSR-Sb.* **73**, 415 (1992).
- ³⁸S. Smale, *Bull. Am. Math. Soc.* **73**, 747 (1967).
- ³⁹S. Smale and M. Shub, *Scholarpedia* **2**, 3012 (2007).
- ⁴⁰S. Gonchenko, L. Shilnikov, and D. Turaev, *Phys. D: Nonlinear Phenom.* **62**, 1 (1993).
- ⁴¹S. V. Gonchenko, L. P. Shilnikov, and D. V. Turaev, *Chaos* **6**, 15 (1996).
- ⁴²S. Jafari, J. Sprott, and F. Nazarimehr, *Eur. Phys. J. Spec. Top.* **224**, 1469 (2015).